الأكاديمية العربية للعلوم والتكنولوجيا والنقل البحري

Arab Academy for Science, Technology & Maritime Transport

## Collage of engineering and Technology

## Mechanical Engineering Department

B. Sc. Final Year Project

# “Plane Air Jet – Surface Water Layer Interaction”


**Submitted By**

Ahmed Diaa

Abdelrhman Ashraf

Yossef Gamal

**Supervised By:**

Dr. Rola Afifi

Dr. kamel elshorbgy

*JULY – 2022*

## *AKNOWLEDGMENT*

*We would like to thank our supervisors, Dr. kamel elshorbgy and Dr. Rola Afify for their support, patience and great knowledge, their guidance us from the beginning till the end we also would like to thank our families for their support and patience. Finally, we really appreciate our collage arab academy for science and technology and maritime transport for being the place where we gained knowledge.*

## *Abstract*

*Jet Impingement Technology (JIT) is widely used as a controller mechanism in various industries. In this paper, a test rig will be presented. Air jet behavior over the impingement region is displayed and discussed. The behavior of the jet exit velocity is checked and the effect of the jet inclination on the wall jet region is illustrated. The velocity profiles are detected at the leading, middle and trailing edges of three different layers. Each layer is observed at four inclination angles of the jet ($\phi$ = 0o , 15o , 30o , 45o ) and three offset ratios of the plate (Z* = 0.5, 2, 3.5).*

# Table of Contents

# Chapter *One*

# INTRODUCTION

## 1.INTRODUCTION

### 1.1. IMPINGING JET

In industrial applications, heat and mass transfer can be considerably increased using impinging jets. Impinging jets can produce very high heat/mass transfer rates since they exhibit amongst the highest known levels of transfer capabilities for single phase flows, especially at low nozzle-to-plate distances [1] [2]. An oriented fluid flow versus a surface can transfer substantial amounts of mass and heat between that surface and the fluid. For example, compared with conventional convection cooling by confined flow parallel to the cooled surface, the use of jet impingement produces in increase in the heat transfer coefficients that are up to three times higher at a given maximum flow speed. Applications to engineering fields include turbine blade cooling [3], paper and fabric drying [4], furnace heating [5], tempering of glass and metal sheets [6] [7], food processing [8] and many others. Heat transfer enhanced by forced convection with impinging jets is known to yield high local and average heat transfer coefficients in the cooling of electronic components [9]. In this field, technological advance relies very much on the ability to dissipate extremely large heat fluxes [10]. Thus, interest in the present topic, from the standpoint of both theoretical and technical assessments,

continues to be unquestioned. The investigation tools, either experimental or numerical, have undergone tremendous developments which allow for a deeper comprehension of the involved phenomena. Since Martin [11] published in 1977 his pioneering review article on heat and mass transfer of impinging jets, several additional literature reviews have appeared [12-15]. In the case of the impinging jet, turbulence is generated by the flow itself and by possible external disturbances and varies significantly with the nozzle shape, the upstream conditions and the position within the jet [16]. The details of the nozzles, and of the upstream flow facility, is important in the design of heat transfer equipment in which turbulent jets impinge at relatively short nozzle-to-plate spacing H/D, but are secondary if impingement occurs beyond H/D > 8(Fig. 1).

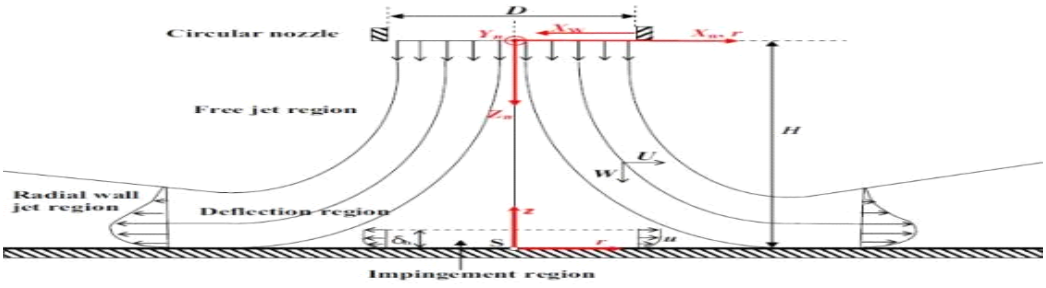


Fig. 1 Schematic description of impinging jet on a flat plate [17]

## 1.2. RECTANGULAR JET

Rectangular jets are used in a growing number of devices – high-speed hand-dryers, car-wind screen heaters, industrial drying units and air conditioning systems to name just some examples. While some research has been conducted on the fluid dynamics of

both plane and rectangular jets, very little work has been undertaken looking at the acoustics of the problem and virtually no work has been undertaken look in gat very high aspect ratio nozzles. Unlike a plane jet (which is constrained by side-walls), a rectangular jet is allowed to spread laterally meaning that the flow-field evolves from being near-two-dimensional at the jet exit to three-dimensional far downstream. This paper presents experimental results from aeroacoustics measurements on high aspect ratio rectangular jets across a range of subsonic Mach numbers .In the 1950s, Coles was leading an investigation for the National Aeronautics and Space Administration(NASA) surrounding the noise benefits, or penalties, associated with using a rectangular jet for aircraft propulsion[18] A full sized aircraft was used as a test bed for this project with a single round nozzle and two rectangular nozzles (aspect ratios AR = 14 and 100) all of equal exit area. Based on Lighthill's work [19] [21] Coles concluded that the sound power from a rectangular jet (of suitably high aspect ratio) should be half that for a round jet of the same exit area (equating to a 3 dB reduction in sound power level). This result was found to be true for the AR = 100 nozzle only. Kouts and Yu [22] experimentally investigated noise from a rectangular jet of aspect ratio AR = 10. They found that the overall sound power level scaled with jet velocity to the 7 and that the slot jet was more effective in radiating higher frequencies than a round jet.

Larsen spent several years researching rectangular jets [23] and in 1984 published a paper with Bjørnø [24] detailing some of the key results. Their research focused on smaller jets using a fixed width of 100 mm with aspect ratios varying from 33.3 to 100. Larsen and Bjørnø developed a theoretical model based on Light hill for the noise intensity radiated from a rectangular jet. This was found to agree well with experimental results for AR &50, however, they note that while the model works well for measurements at large angles to the jet axis, it overestimates the sound radiation at smaller a Virtually all investigations into rectangular and plane jets have been performed with jet aspect ratios AR .100. The only significant work for AR >100, is that by Munro and Ahuja [25] who, as part of a wider investigation into circulation control wings, investigated the acoustics and fluid dynamics of high aspect ratio nozzles (100 <AR

<3000). The authors drew comparisons between their investigation and the work of others, notably Larsen [23] [24]and Tam et al [25] [27] on the chosen length scales for the analysis. For the acoustics Munro and Ahuja propose a similar noise model to Larsen and Bjørnø this time based on an equivalent length Leq =hnwm (where n+m= 1 and w is the width of the jet). From their results, they determined that the best fit for the noise data to collapse occurs with L2eq = (h3/4w1/4)2, in contrast to Larsen and Bjørnø [7] who found L2eq =hw. gles.

The most recent acoustics investigations have been performed by Kanjere et al. [28] who found that the sound power from a rectangular jets scales with jet velocity to the 7 – matching the earlier result of Kouts and Yu [22]

While the acoustics has seen a relatively small amount of research performed on it, the fluid dynamics have been more widely researched. In addition to the work of Munro and Ahuja, the combined works of Deo, Mi and Nathan [29] [34] provide a wealth of material on the fluid dynamics of plane and rectangular jets. The majority of their experiments were performed using a hotwire anemometer investigating aspect ratios in the range 15 ≤AR ≤72 across Reynolds numbers 1500. Reh.6×104. Although no consideration is given to acoustics, the work is nonetheless informative, as understanding the fluid behavior is key to accurately determining the source mechanisms.

Deo et al. have presented results detailing the dependence of a plane jet on aspect ratio, [31] Reynolds Number [33] and nozzle inlet profile. [32] Building on the earlier work of Quinn, [35] the group concluded that all normalized mean and turbulent properties of a plane jet are dependent on nozzle aspect ratio; however, much larger aspect ratios would need to be tested for an asymptotic independence to be identified. They also suggest that any large scale structures within the jet may be aspect ratio dependent. This conclusion was reached by noting that the overall spreading and decay rates are themselves aspect ratio dependent and are physically governed by large scale structures in the jet

For the Reynolds number dependence, [33] the authors conclude that plane jets are dependent on Reynolds numbers for Reh≤2.5×104and the effect is substantial for Reh≤1×104. They note that, for increasing Reh, the near-field spreading rate increases, while the potential core length, the far-field mean velocity decay rate and the far-field spreading rate all decrease. They also provide some results into coherent structures in plane jets, concluding that the symmetric mode dominates at Reh= 1500, the antisymmetric mode dominates for Reh≥1×104, while between 1500 <Reh<1×104, both modes are present with neither dominating. The symmetric and antisymmetric modes have also been referred to as ‘puffing’ and ‘flapping ’in previous work [36].

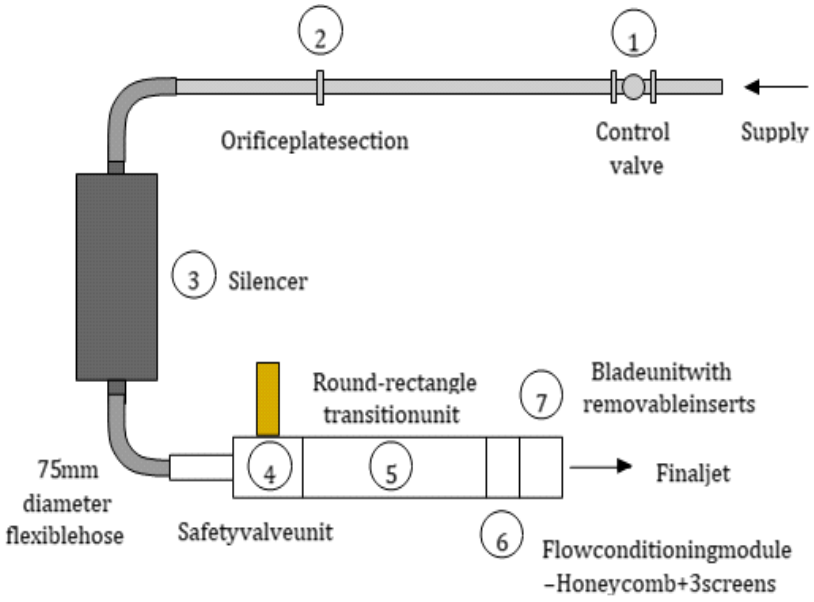


Figure 2: Overall layout of the experimental rig and air supply

When investigating the turbulent properties, [30] Mi et al. concluded that a turbulent rectangular jet of sufficiently high aspect ratio (AR & 15) has three distinct flow regions – an initial quasi-plane-jet region where UCL ≈ constant, a transitional region where UCL ~ x −1/2, and a final quasi-axisymmetric-jet where UCL ~ x −1 (where x is the downstream

distance and UCL is the centerline velocity). The authors conclude that the rectangular jet can be approximated to a plane jet in the first region only and that the axial extent of this first region increases with aspect ratio. This is in direct contrast to Quinn [35] who found that the nearfield mixing in rectangular jet flows increases with increasing nozzle aspect ratio and that shorter potential core lengths are found in the higher aspect ratio jets. For changes in nozzle profile [32] Deo et al. found that the exit velocity profile varied from being 'saddle backed' for small inlet radii (typically $r/h \leq 0.9$), to more 'top-hat' like for larger inlet radii. Additionally, it was found that, for increasing r/h, the initial boundary layer thickness increased, while the near-field vortex shedding frequency and the peak turbulence intensity both decreased. An asymptotic decrease was observed for the centerline velocity decay rate, the jet spreading rate and the far-field turbulence intensity. Deo et al. state that their results [31] [33] back up the hypothesis of George [37] and George and Davidson [38] that the downstream development of a plane jet is entirely dependent on the initial conditions. However, for a round jet, Jordan and Colonius [39] state that there is disagreement on this subject. From the literature it can be concluded that little work has been performed on the acoustics of rectangular and plane jets, particularly for AR & 100. From the work on the fluid dynamics of the problem, it can be concluded that the development of the jet can be split into three main regions and that the nozzle geometry and aspect ratio play an important role in establishing the normalized mean and turbulent properties of the jet. The limited volume of work suggests however that there is some disagreement on the relevant length scale for these jets. The aim of this paper is to present results from a series of experiments investigating the acoustic characteristics of rectangular nozzles and the fluid behavior that leads to the measured sound-field. The remainder of the present paper is structured as follows. First we briefly describe the experimental rig and setup used in the investigations in section II; before moving on to the results for fluid dynamics (section III) and acoustics (section IV). Finally, sections V and VI draw some conclusions and highlight areas for future work.

## 1.3. Coanda effect

The tendency of a jet of fluid emerging from an orifice to follow an adjacent flat or curved surface and to entrain fluid from the surroundings so that a region of lower pressure develops Coanda effect is the phenomena in which a jet flow attaches itself to a nearby surface and remains attached even when the surface curves away from the initial jet direction. In free surroundings, a jet of fluid entrains and mixes with its surroundings as it flows away from a nozzle.

When a surface is brought close to the jet, this restricts the entrainment in that region. As flow accelerates to try balance the momentum transfer, a pressure difference across the jet results and the jet is deflected closer to the surface - eventually attaching to it. Even if the surface is curved away from the initial direction, the jet tends to remain attached. This effect can be used to change the jet direction. In doing so, the rate at which the jet mixes are often significantly increased compared with that of an equivalent free jet. The phenomena derive its name from a Romanian born aeronautical engineer - Henri Coanda.

In 1910, Coanda designed and built what was arguably the world's first jet propelled aircraft. The plane used a 4-cylinder piston engine to power a rotary compressor. The compressor exhaust entered two ring-shaped burning chambers located on each side of the fuselage. The gasoline engine's exhaust and additional fuel was also ported into the chambers. The combustion of this mixture exhausted from the chambers down the steel-sheeted plywood sides of the Coanda-1910 producing a thrust of 220 kgf. He performed the first reactive flight on 16 December 1910 - which unfortunately ended in an accident. After the plane took off, Coanda observed that the flames and burned gases exhausted from the engine "hugged" the fuselage and the aircraft side rapidly caught fire. After studies which lasted more than 20 years, the phenomenon was recognized as a new aerodynamic effect: The Coanda effect. Many devices use Coanda effect. One notable application of the Coanda effect is the helicopter. NOTAR (No TAil Rotor) is the name of a helicopter system which replaces the use of a tail rotor. The system uses a fan inside the tail boom to build a high volume of low-pressure air, which exits through two

slots and creates a boundary layer flow of air along the tail boom utilizing the Coanda effect. The use of directed air to provide anti-torque control had been tested as early as 1945 in the British Cierva W.9. There are three production helicopters that utilize the NOTAR system, all produced by MD Helicopters.

### 1.3.1.Test Procedure

In order to establish the different flow regimes associated with the plane air jet impinging on a flat plate, the following experiment steps are carried out: Adjustment of geometrical parameters to the required settings, shown in Fig.3. They include inclination angles $\phi = 0^o, 15^o, 30^o, 45^o$, offset ratios Z* = (/t) = 0.5, 2, 3.5, and the impinging plate's horizontal mounting.

- Measurement of ambient conditions; pressure ($P_{atm}$) and temperature ($T_{atm}$).
- Start the air flow at a desired Reynolds number $R_{ej}$; through adjustment of the corresponding pressure regulator reading. Wait until steady state condition is established. Steady state condition and $R_{ej}$ value are to be checked by measuring the center line jet exit velocity at nozzle mouth $U_j$. In the present experiment, the value of Reynolds number is selected as Rej ≈ 1500.
- Measurement of reattachment distance $X_R$, to avoid recirculating regions, Fig.4, by moving the Pitot tube gradually along the center line of the impinging plate with a verified notation that the probe is tangent to the plate. Until the manometer reading just exceeds the zero reading. The horizontal distance between the probe nose at this location and the point vertically viewed from the nozzle exit midpoint represents the reattached distance $X_R$.
- Using Pitot tube traverses measurements are made of velocity distributions U = U(Z) at different stations, as shown in Fig 4. In order to conform to experiments, the selected stations were therefore related to the size of considered layers there (256 x 50, 256 x 128, and 256 x 256). Nominally three station for each layer are considered (leading edge "L.E.", middle of layer "M.L.", and trailing edge "T.E."), as shown in Fig.5. Table 1 shows the test locations (X) for each layer. These stations are selected with a

separation distance (25, 64, and 128 mm respectively) to define accurately the wall jet regime related to certain values of $R_{ej}$, ϕ, Z*.

- Repeat of steps 1, 2, 4, and 5 for other values of ϕ, Z*.

## 1.3.2.Discussion

Table 2 shows the corresponding reattachment distances ($X_R$) for each layer. These cases resulted in the velocity distribution for impingement region; one can accurately define the wall jet region for each package combination of, Z*, $R_{ej}$. The results of velocity distribution for all investigated cases, the dimensionless local velocity $U/U_{max}$ is plotted against the dimensionless vertical height from the level of the horizontal plate (wall), Z/t. It is important to refer here to the test case (= $0^o$, Z* = 0.5) as a reference in all test cases, in which the flow is entirely a pure wall jet, figures (9, 21, 33), for different layer dimensions. The results, in all figures, were terminated at a definite value ($U/U_{max}$ = 0.1). At this value of $U/U_{max,}$ the inclined manometer used for measuring the dynamic head gives no accurate but fluctuated reading. This is, however, expected to occur due to entrainment process at the jet boundaries

**Table 1. Experimental stations' locations (X) in mm for each layer**

| Layers | Layer dimensions | | |
|---|---|---|---|
| Name | x 50 256 | x 128 256 | x 256 256 |
| .L.E | 150 | 111 | 47 |
| .M.L | 175 | 175 | 175 |
| .T.E | 200 | 239 | 303 |

**Table 2. Experimental reattachment locations ($X_R$) in mm for different inclination angle .($\phi$), offset different offset ratio (Z*), and $R_{ej}$ = 1500**

| Z* \ϕ | 0° | 15° | 30° | 45° |
|---|---|---|---|---|
| 0.5 | 0 | 0 | 0 | 0 |
| 2 | 16 | 14 | 3 | 1.5 |
| 3.5 | 34 | 27 | 12 | 2 |

Important conclusion derived is that in the presence of streamline curvature, the pressure decreases with increasing radial distance from the center of curvature. This is strongly manifested in some types of environmental flow resulting in what is known as the Coanda effect, named after Henri Marie Coanda (1885–1972), a Romanian aeronautical engineer who made major contributions to aircraft technology.

A free jet of air entrains molecules of air from its immediate surroundings causing an axi symmetrical "tube" or "sleeve" of low pressure around the jet The resultant forces from this low pressure tube end up balancing any perpendicular flow instability, which stabilizes the jet in a straight line. However, if a solid surface is placed close, and approximately parallel to the jet then the entrainment (and therefore removal) of air from between the solid surface and the jet causes a reduction in air pressure on that side of the jet that cannot be balanced as rapidly as the low pressure region on the "open" side of the jet. The pressure difference across the jet causes the jet to deviate towards the nearby surface, and then to adhere to it The jet adheres even better to curved surfaces because each (infinitesimally small) incremental change in direction of the surface brings about the effects described for the initial bending of the jet towards

the surface If the surface is not too sharply curved, the jet can, under the right circumstances, adhere to the surface even after flowing 180° round a cylindrically curved surface, and thus travel in a direction opposite to its initial direction. The forces that cause these changes in the direction of flow of the jet cause an equal and opposite force on the surface along which the jet flows. These Coandă effect induced forces can be harnessed to cause lift and other forms of motion, depending on the orientation of the jet and the surface to which the jet adheres A small "lip" on the surface at the point where the jet starts to flow over that surface enhances the initial deviation of the direction of flow of the jet, and it subsequently adheres to the surface. This results from the fact that a low pressure vortex forms behind the lip, promoting the dip of the jet towards the surface.

The Coanda effect can be induced in any fluid, and is therefore equally effective in water as in air. A heated airfoil significantly reduces drag

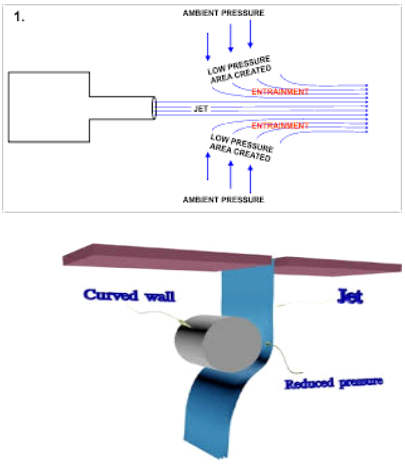


Fig3&4

## 1.4. Experimental study

The experimental facility used to perform the visualizations is presented in Fig. 5a. The impingement plate used for the tests is a $3\ mm$ thick smooth Plexiglas plate whose vertical position can be modified to allow the change of the nozzle-to-plate distance. The air jet is formed by the submerged injection of air through a circular nozzle (Fig. 5b). Four jet nozzles with different inner diameters (

$4.8, 10, 12.4, 19.2\ mm$) are used. They are obtained from PLA thermoplastic material, by using a 3D printer. The jet settling chamber has a volume of $170\ dm^3$. The air is seeded with particles using a smoke machine Showtec Atmos 1000 and is sent inside the settling chamber and then through the jet nozzle by a fan with adjustable speed. A continuous wave laser with $532\ nm$ wavelength, equipped with a cylindrical lens to convert the beam in a planar sheet, is then lighting the impinging jet through its axis in order to make it visible. The laser beam is reflected by a mirror to increase the lighting power in the area where the jet hits the wall. The dynamics of the impinging jet is recorded with a Nikon 1 J5 camera at $400\ fps$ and a resolution of $800 \times 296$ pixels. The camera is placed perpendicular to the plane lighted by the laser sheet, so that the focus is made on the zone between the nozzle mouth and the impingement plate.

The mean jet velocity was measured as the distance traveled by the fluid in a known time period. The distance between the nozzle mouth and the solid wall is rigorously set and is taken as reference, as for the time, it is inferred from the camera framerate.

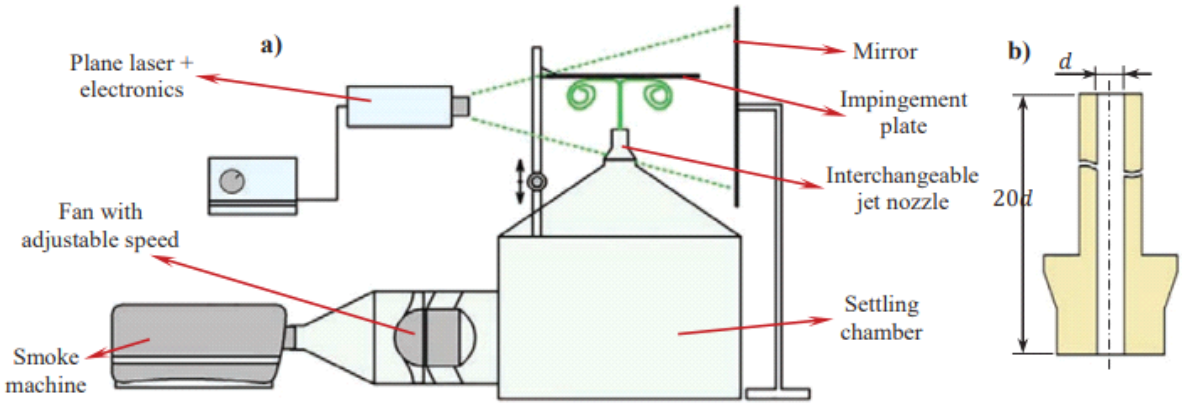


Fig. 5. Sketch of experimental set-up (a) and sketch if typical jet nozzle used in experiments (b).

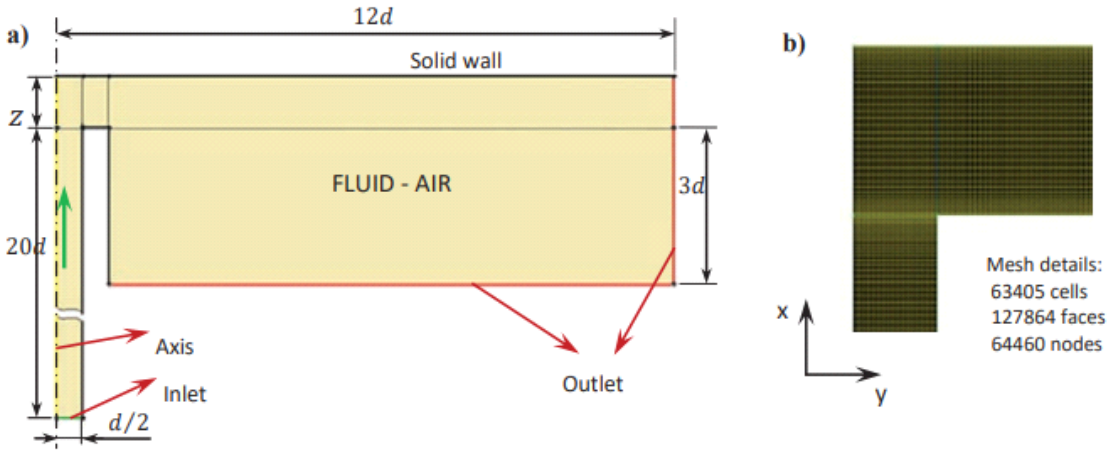


figure. 6. Numerical flow domain with boundary conditions (a) and detail of mesh in the impingement zone (b).

### 1.4.1. Numerical domain and boundary conditions

The objective of the CFD study is to provide a closer touch with the numerical approach by analyzing the flow configuration of a laminar flow impinging over a plate, in similar cases to the ones experimentally analyzed. Hence, a comparison with experimental results will be presented. The numerical simulations are carried out by using the commercial software Fluent, developed by ANSYS, in the context of Reynolds-averaged Navier-Stokes (RANS) modeling. The Fluent solver is based on a finite-volume solution of the mean momentum, energy and turbulent transport equations. The scheme selected to perform all the computations is second order upwind.

This case was modeled using the axis symmetry condition. In Fluent, axis-symmetric indicates that the flow domain is symmetric around the $x$ axis, like described in reference [50]. The domain was built according to this condition. When axis-symmetry condition is enabled, the 2D axis-symmetrical form of the governing equations is solved instead of the 2D Cartesian form.

The geometrical dimensions of the domain defined for computations are dependent on the nozzle diameter and the nozzle-to-plate distance. The outlet border should be placed at a sufficiently large radial distance, so that error arising from the application of outlet-pressure condition will not significantly affect the region of interest. According to the references [51] and [52], the radial expansion of the flow domain was chosen at 12d.

In order to achieve a fully developed flow at the nozzle exit, a pipe section with a length of 20d was added to the domain. Another consideration is about the vertical distance from the nozzle mouth to the lower boundary of the domain, as from the latter some flow entrainment can occur. Then, a sufficient large distance between the two is necessary in order to limit boundary influences. A three nozzle diameters distance from the nozzle mouth to the lower boundary was selected. A schematic view of the computational domain characteristics is presented in Fig. 5a. A detail of the mesh used and the mesh characteristics are shown in Fig. 5b.

Table 1 shows the test cases that are simulated numerically. The three parameters: jet standoff distance z/d, Reynolds number Re and jet diameter d are considered.

Table 1. Numerical test matrix for the case in study.

| | $z/d = 1$ | $z/d = 2$ | $z/d = 4$ | $z/d = 6$ | |
|---|---|---|---|---|---|
| $Re = 300$ | $d_1$ | $d_1$ | – | – | $d_1 = 4.8\ mm$ |
| $Re = 420$ | $d_1$ | $d_1$ | $d_1$ | $d_1$ | $d_2 = 10\ mm$ |
| $Re = 600$ | $d_1$ | $d_1$ | – | – | $d_3 = 12.4\ mm$ |
| $Re = 1000$ | $d_1$ | $d_1, d_2, d_3,$ | – | – | $d_4 = 19.2\ mm$ |

## 1.4.2. Experimental results

The growth of the Kelvin–Helmholtz instabilities in the shear layer leads to the formation of roll-up vortices (Fig. 6a) with a natural frequency characterized by the Strouhal number St defined in terms of mean jet velocity v and nozzle diameter d. Periodic formation and breakdown of the side vortices lead to pressure pulsation in the jet irrespective of whether it is laminar or partially turbulent. In the jet developing zone, the axial velocity decreases as a result of radial spreading due to a strong shear at the jet boundary and the entrainment of surrounding fluid

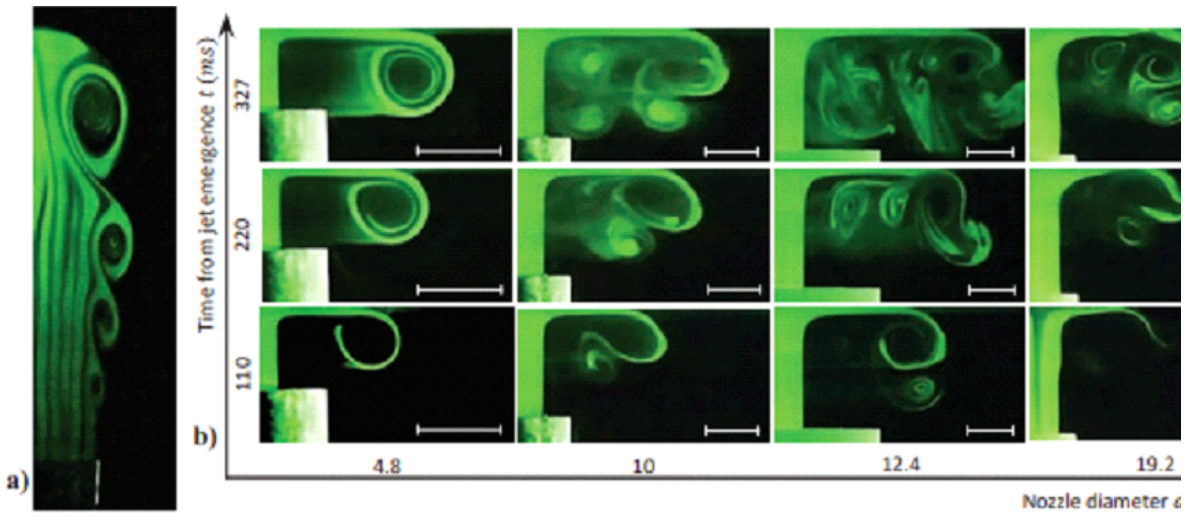


Figure8 Side vertices in the free jet region for z/d>>1(a);

Time evolution of impinging jet for different nozzle diameters, z/d=2. Scale bars represent 10 mm (b).

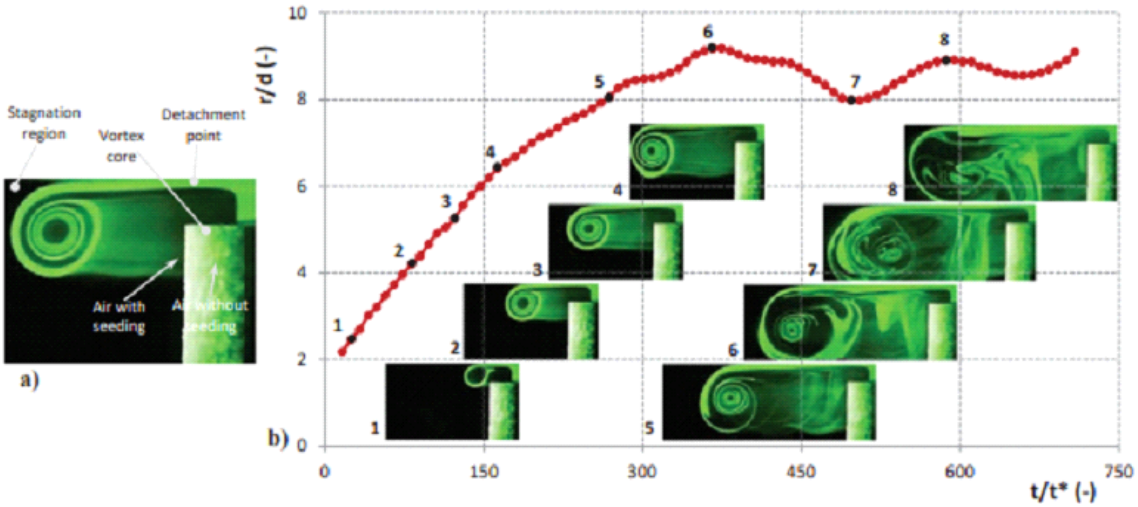


Fig.9 Specific points and regions of the vortex ring and typical fluid layers in the vortex (a):

Time evolution of vortex radial development for Rc=420, d=4.8 mm, zz/d=1(b)

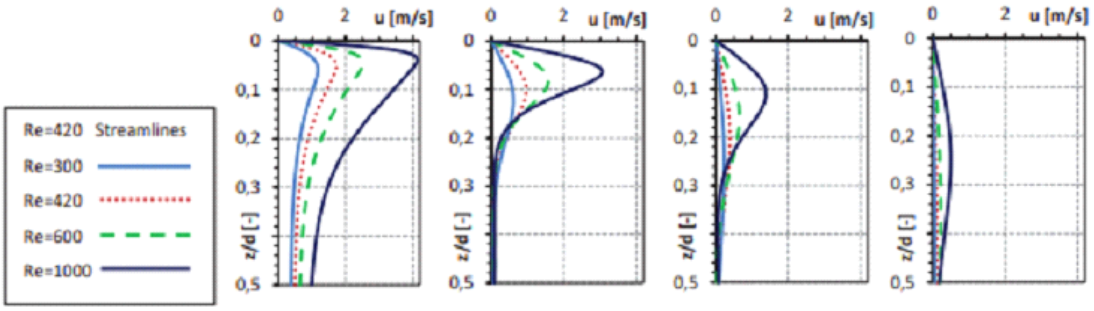


fig.10 Flow field for Re=420 at steady state and radial velocity profiles in the near-wall region for various Reynolds number

As the jet approaches the wall, its presence begins to affect the velocity and stress fields. A stagnation region is formed in the center of the impingement zone. Due to the presence of the solid impermeable wall, the axial velocity diminishes fast, followed by an increase of the static pressure [40]. After hitting the wall, the jet deflects to radial direction and a wall-jet is formed further downstream.

Around the jet deflection region, corresponding to the maximum streamline curvature, the accelerating boundary layer becomes thinner – see the streamlines distribution in Fig. 5, in the interval r/d =1...3. Eventually, it evolves into a radial wall-jet where the fluid

is decelerated because of the radial spreading. The wall-jet is characterized by a strong shear with the turbulence level much higher than in an ordinary boundary layer [47].

After hitting the wall, as the direction of the jet changes to radial, a vortex ring begins to form. The ejected fluid enters the ambient fluid. The vortex core and the detachment point from the wall (Fig. 7a) are qualitatively inferred from the experimental pictures. As the vortex rolls up and develops, the different layers of air with seeding, as well as entrained air without seeding (Fig. 7a), are visible in the plane of the laser light.

The vortex evolution is presented in Fig. 4b. Pictures taken at different time instants can be seen, together with a graph showing the progress in time of the vortex core radial position. The time axis is normalized with t, defined as the ratio between the jet diameter d and the mean flow velocity v. This evolution has a quasi-linear trend for r/d<8 ,, then an oscillatory character around the mean value of r/d =8.5 is observed.

As a consequence of the increase in standoff distance z/d, the jet starts to flap and the stagnation point changes in time around the geometrical center.

## 1.5. EVAPORATION

Evaporation is a type of vaporization that occurs on the surface of a liquid as it changes into the gas phase. The surrounding gas must not be saturated with the evaporating substance. When the molecules of the liquid collide, they transfer energy to each other based on how they collide with each other. When a molecule near the surface absorbs enough energy to overcome the vapor pressure, it will escape and enter the surrounding air as a gas. When evaporation occurs, the energy removed from the vaporized liquid will reduce the temperature of the liquid, resulting in evaporative cooling.

On average, only a fraction of the molecules in a liquid have enough heat energy to escape from the liquid. The evaporation will continue until an equilibrium is reached when the evaporation of the liquid is equal to its condensation. In an enclosed environment, a liquid will evaporate until the surrounding air is saturated.

Evaporation is an essential part of the water cycle. The sun (solar energy) drives evaporation of water from oceans, lakes, moisture in the soil, and other sources of water. In hydrology, evaporation and transpiration (which involves evaporation within plant stomata) are collectively termed evapotranspiration. Evaporation of water occurs when the surface of the liquid is exposed, allowing molecules to escape and form water vapor; this vapor can then rise up and form clouds. With sufficient energy, the liquid will turn into vapor.

For molecules of a liquid to evaporate, they must be located near the surface, they have to be moving in the proper direction, and have sufficient kinetic energy to overcome liquid-phase intermolecular forces. When only a small proportion of the molecules meet these criteria, the rate of evaporation is low. Since the kinetic energy of a molecule is proportional to its temperature, evaporation proceeds more quickly at higher temperatures. As the faster-moving molecules escape, the remaining molecules have lower average kinetic energy, and the temperature of the liquid decreases. This phenomenon is also called evaporative cooling. This is why evaporating sweat cools the human body. Evaporation also tends to proceed more quickly with higher flow rates between the gaseous and liquid phase and in liquids with higher vapor pressure. For example, laundry on a clothes line will dry (by evaporation) more rapidly on a windy day than on a still day. Three key parts to evaporation are heat, atmospheric pressure (determines the percent humidity), and air movement.

On a molecular level, there is no strict boundary between the liquid state and the vapor state. Instead, there is a Knudsen layer, where the phase is undetermined. Because this layer is only a few molecules thick, at a macroscopic scale a clear phase transition interface cannot be seen

Liquids that do not evaporate visibly at a given temperature in a given gas (e.g., cooking oil at room temperature) have molecules that do not tend to transfer energy to each other in a pattern sufficient to frequently give a molecule the heat energy necessary to turn into vapor. However, these liquids *are* evaporating. It is just that the process is much slower and thus significantly less visible.

Evaporative equilibrium

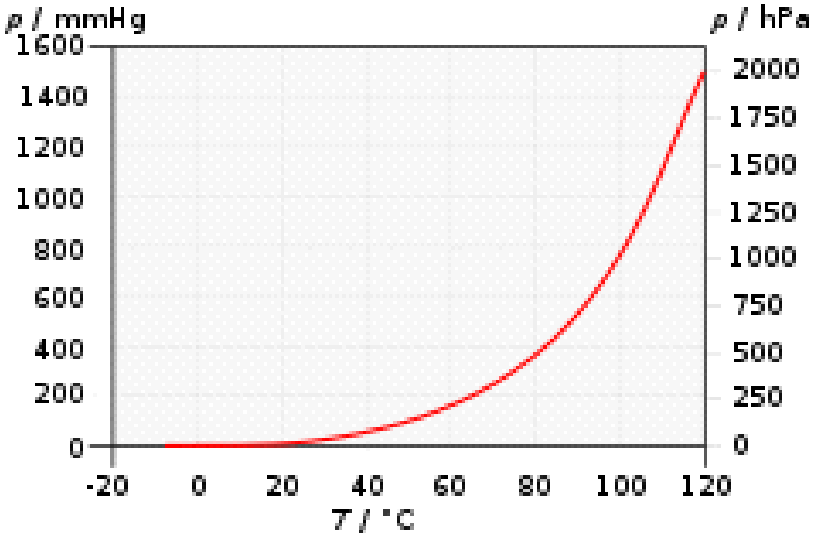


Vapor pressure of water vs. temperature. 760 Torr = 1 atm.

If evaporation takes place in an enclosed area, the escaping molecules accumulate as a vapor above the liquid. Many of the molecules return to the liquid, with returning molecules becoming more frequent as the density and pressure of the vapor increases. When the process of escape and return reaches an equilibrium, the vapor is said to be "saturated", and no further change in either vapor pressure and density or liquid temperature will occur. For a system consisting of vapor and liquid of a pure substance,

this equilibrium state is directly related to the vapor pressure of the substance, as given by the Clausius–Clapeyron relation:

where $P_1$, $P_2$ are the vapor pressures at temperatures $T_1$, $T_2$ respectively, $\Delta H_{vap}$ is the enthalpy of vaporization, and $R$ is the universal gas constant. The rate of evaporation in an open system is related to the vapor pressure found in a closed system. If a liquid is heated, when the vapor pressure reaches the ambient pressure the liquid will boil.

The ability for a molecule of a liquid to evaporate is based largely on the amount of kinetic energy an individual particle may possess. Even at lower temperatures, individual molecules of a liquid can evaporate if they have more than the minimum amount of kinetic energy required for vaporization.

## Factors Influencing the rate of evaporation.

Note: Air used here is a common example; however, the vapor phase can be other gases.

- Concentration of the substance evaporating in the air

If the air already has a high concentration of the substance evaporating, then the given substance will evaporate more slowly.

- Flow rate of air

This is in part related to the concentration points above. If "fresh" air (i.e., air which is neither already saturated with the substance nor with other substances) is moving over the substance all the time, then the concentration of the substance in the air is less likely to go up with time, thus encouraging faster evaporation. This is the result of the boundary layer at the evaporation surface decreasing with flow velocity, decreasing the diffusion distance in the stagnant layer.

The amount of minerals dissolved in the liquid

- Inter-molecular forces

The stronger the forces keeping the molecules together in the liquid state, the more energy one must get to escape. This is characterized by the enthalpy of vaporization.

Evaporation happens faster if there is less exertion on the surface keeping the molecules from launching themselves.

- Surface area

A substance that has a larger surface area will evaporate faster, as there are more surface molecules per unit of volume that are potentially able to escape.

- Temperature of the substance

The higher the temperature of the substance the greater the kinetic energy of the molecules at its surface and therefore the faster the rate of their evaporation.

In the US, the National Weather Service measures the actual rate of evaporation from a standardized "pan" open water surface outdoors, at various locations nationwide. Others do likewise around the world. The US data is collected and compiled into an annual evaporation map. The measurements range from under 30 to over 120 inches (3,000 mm) per year.

Because it typically takes place in a complex environment, where 'evaporation is an extremely rare event', the mechanism for the evaporation of water isn't completely understood. Theoretical calculations require prohibitively long and large computer simulations. 'The rate of evaporation of liquid water is one of the principal uncertainties in modern climate modeling

## Discussions

Investigated Reynolds number of evaporation is chosen to achieve the goal of the present study, since the evaporation tests are carried out for water layers of constant height of 3mm and constant hydrodynamic physical regime for the present tests. To avoid the trailing edge ejection of the water layer, we take into consideration the high sensitivity to air flow exposure of the water layer (relatively large thickness of 3mm). All the tests are carried out to begin with the vortex motion regime. For all test cases the layer height H is 3mm at the starting time of evaporation, and the flow regimes begin with vortex motion. The vortex motion is noticed by the means of adding micro balloons to the water layer surface. As soon as the air jet starts blowing the micro balloons begin

to rotate in two opposite directions, see Figs. 6(a, b, c) and 7 (a, b, c). As the evaporation progresses and the water layer height decreases, the vortex motion rotation is observed to decrease and the small waviness associated with the vortex motion turned to large scale disturbances. Higher evaporation rates are observed to occur with time. The vortex motion is seen to appear semi stagnant. Large scale disturbances turned out to small scale disturbances. Finally, the vortex motion stopped and the layer stayed semi stagnant where a thin film region is achieved. Evaporation continues with time, without change in the layer dimensions except thickness or height which was recorded to decrease for approximately more than 90% of the total evaporation time of the layer. This observed phenomenon is different from the previous observations of Elshorbagy and Khalil who noticed the drop diameter to decrease with time throughout evaporation. While in evaporation phenomenon was very near to the present study. Radwan related the difference between his phenomenon in evaporation and Elshorbagy and Khalil phenomenon to the difference between the flat plate material used by Elshorbagy and Khalil (ordinary glass) and that used in his experiments and also in the present study (plexi glass). Such difference is associated with differences in surface tension, either between gas-solid or between liquid-solid, as a result of the different surface textures of these plates. Also the drop size and shape may affect such disagreement; Radwan stated another important reason that liquid drops in the literature assumed part of semi spherical shape, without restrictions to their heights. Such spherical shape should redistribute both of normal and shear stresses in a different manner that leads to drop diameter shrinkage. For the present investigation, one can observe the same type of shrinkage achieved with Radwan, i.e. flat surface type shrinkage, which usually occur in the last 10% from the total evaporation time of the water layer. Fig. 6and7, show the layer when it attains its thin film region followed by surface shrinkage for the water layers. Shrinkage of the layers appears at the leading edge and continue gradually till full evaporation of the layer is achieved. The shrinkage is observed to usually occur in two places: either in the middle of the layer at the leading edge or at the vortex stream from the leading edge side. Fig. 8(d) shows shrinkage

occurrence at the leading edge in the vortex stream. The shrinkage increases to take the crescent shape at the leading edge. This crescent shape is observed clearly in the (256 x 128 mm) and (256 x 256 mm) water layers, Fig. 8 (e) and Fig. 9 (e and f). However, in the case of (256 x 50 mm) water layer, shrinkage occurs in the middle of the layer at the leading edge. This causes the layer to be separated into two parts quickly, since these slices are so limited in their dimensions in the stream wise direction, or in x direction, Figs. 6 and 7. However, when shrinkage from the leading edge at the middle or at the vortex stream begins, it continues gradually in the form of a crescent until complete evaporation is achieved. It must be mentioned that the present study has the same type of shrinkage with Radwan (surface type shrinkage) but not in the same manner. The shrinkage in Radwan study is associated with evaporation from the leading edge which was achieved with diameter variation (circular thin film shrinkage), Fig. 10. In the present study, the layer took the shape of crescent from the early beginning of evaporation (crescent surface type shrinkage),

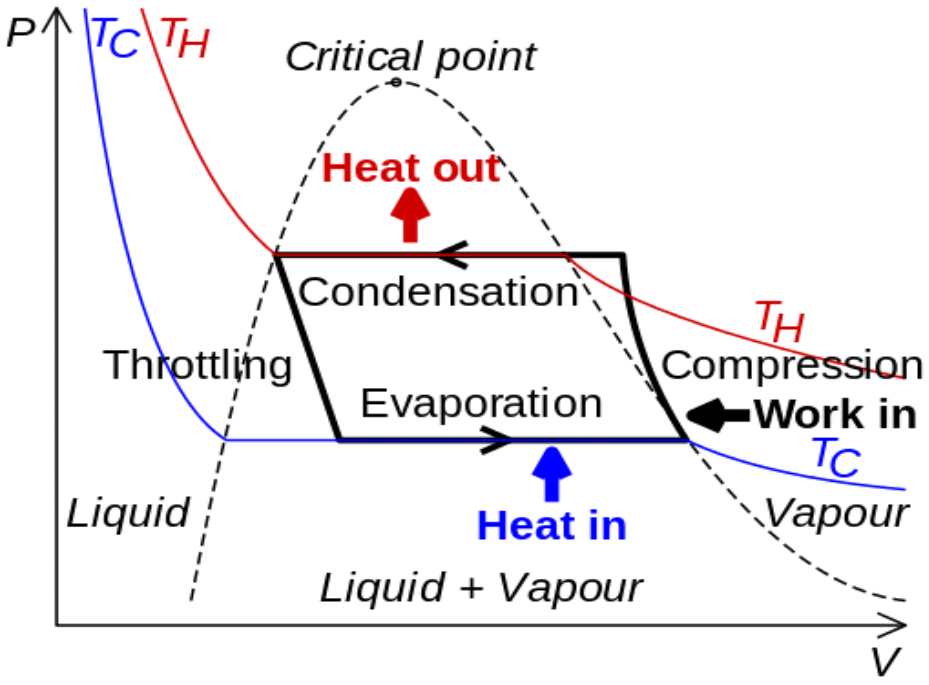
P
$T_C$
$T_H$
Critical point
Heat out
Condensation
$T_H$
Throttling
Compression
Evaporation
Work in
$T_C$
Liquid
Heat in
Vapour
Liquid + Vapour
V

Fig. 11

## 1.6. Flow regime patterns

Multiphase flows are considered as complicated flow phenomena compared to a single flow [45]. There are essential features of multiphase flows whose modeling outcome is contentious and structural explanation is still unexplored. The most common type of multiphase flow in almost all chemical, petroleum, and production industries is the two-phase gas/liquid flow [46,47]. Different forms of flow patterns may be observed when two or more phases flow simultaneously [46]. In pipe cross-sections, unpredictable turbulent flow structures generating highly asymmetric volume distribution are a challenge in experiential investigations [47,48]. This kind of unstable flow condition complicates the measurement process and may create difficulties in capturing actual flow conditions. There are also instances where the existing theoretical solution or experimental results cannot describe specific physical properties [45,49].

Flow regimes or patterns are amongst the most significant aspects of multiphase flow. The structural flow distribution of different phases in a pipe is known as the flow pattern or flow regime. The flow regime depends on the inertia force, buoyancy force, flow turbulence, and surface tension, which are altered by fluid properties, flow rates, pipe diameter, and pipe predilection [50,51]. Different forms of flow patterns may be observed when two phases of gas/Newtonian and gas/non-Newtonian flow simultaneously. Some of the conventional distributions are stratified flow, where the liquid and gas phase is separated, and the gas flows on top as it is lighter than the liquid; bubbly flow, where there is a dispersion of small-sized bubbles within the liquid; slug flow, in which each gas bubble forms a large slug shape (often a bullet shape); and annular flow where liquid flows as a film on the wall of the pipe. For gas/Newtonian and gas/non-Newtonian flow, several flow maps exist to predict the flow patterns. The Taitel and Dukler [51] and Mandhane et al. [53] flow maps for gas/Newtonian flow, and the Chhabra and Richardson [54] flow map for gas/non-Newtonian flow are the most frequently used.

Among the flow regimes, slug flow is the most frequent two-phase flow phenomena experienced in horizontal or near horizontal pipelines in practical applications [55–57].

The presence of slug flows in a pipeline can trigger a great range of design and operational problems, including the exertion of kinetic force on fittings and fittings, pressure cycling, control instability, and inadequate phase separation. If the flow rate is raised, much of the liquid is swept out, and the liquid handling capacity of the receiving facilities may be overwhelmed. In the case of a slug greater than the slow catcher capacity, the facilities can be flooded and destroyed. Therefore, multiple operational problems, such as pipeline network instability and damage to equipment due to high-pressure fluctuation or vibration of the system, can be caused by slug flow [58,59]. This can also be termed a water hammering effect. Therefore, slug flow and slug frequency analysis has been one of the primary research interests in multiphase flow.

To measure the hydrodynamic behavior of multiphase flow, it is essential to understand flow pattern under specific flow conditions [46,60]. Two-phase flow implies gas and liquid flow through a pipeline system, simultaneously. The gas and liquid interface is deformable, so it is hard to predict the region occupied by a gas or liquid phase [61]. When two phases flow through a pipeline, different types of interfacial distribution can form. The variety of flow patterns mostly depends upon the input flux of the two phases, the size and assembly of the pipe, the physical properties of the fluid, etc. Many experimental studies on gas/Newtonian or solid/Newtonian fluid flow have been conducted [62–68]. Nevertheless, a limited number of studies have observed non-Newtonian multiphase flow [69,70].

Xanthan gum is the most commonly used industrial biopolymer for thickening and stabilizing an aqueous system. Xanthan gum solution has significant thermal stability with pseudo plastic properties [71]. Due to these properties, it has a substantial application in petroleum industries. In oil industries, xanthan gum is widely used in drilling fluid [72]. Xanthan gum is also broadly used in the food industry, cosmetics, and pharmacological products [71,73].

Tutu [74] and Drahos et al. [75] characterized two-phase horizontal flow regime pressure fluctuation. Drahos et al. [76] used a probability density function (PDF), where a strain gauge pressure transducer was used in a 50 mm inner diameter (ID) Perspex pipe. Sun et

al. [77] used norm entropy wavelet decomposition to analyze gas/liquid two-phase flow pressure signal data across a bluff body. Here, the inner pipe diameter was 50 mm, and, from a piezo resistive differential pressure sensor, the pressure signals were analyzed using four levels and four scales of Daubechies wavelet (db4), which provided 16 wavelet packet coefficients. This study [76] also suggested an entropy-based two-phase flow map with an identification rate of 95%. Blaney [77] used gamma rays to identify flow regimes, and continuous wavelet transforms to analyze gamma count data. Park and Kim [78] applied the wavelet packet transform to analyze pressure fluctuations in a vertical bubble column.

Furthermore, De Fang et al. [79] also used wavelet analysis to understand the gravity differential pressure fluctuation signal perpendicular to the horizontal flow of different flow patterns and the flow pattern transition of gas/liquid two-phase flow in the horizontal pipe. Here, the Haar wavelet with six levels was used to decompose the pressure signal, and the energy value was then obtained for each scale. For identifying a two-phase flow regime, Elperin and Klochko [80] also used an eight-level db4 wavelet transformation to process time series of the measured differential pressure fluctuation. In this study, using pressure transducer signal data of different flows, the pattern was analyzed using wavelet transformation to determine the pressure signal characteristics of various flow regimes.

To identify the two-phase flow regime mapping and avoid slug flow in horizontal pipelines, a clear understanding of the Newtonian and non-Newtonian fluid flow is necessary for an accurate and inherently safer design for any flow system. The uniqueness of this study is that the experiments were performed in a setup with 73.66 mm ID and approximately 19 m flow loop in the presence of gas/Newtonian and gas/non-Newtonian two-phase horizontal flow. This flow loop has a horizontal, vertical, and inclined test section connected; however, the study is only on horizontal flow aspects. Another primary focus of this study is to understand the characteristics of slug frequency analysis for both air/Newtonian and air/non-Newtonian flow conditions in the presence of Xanthan gum as a non-Newtonian fluid. This study also recognizes the

characteristics of wavelet analysis for both air/Newtonian and air/non-Newtonian flow conditions, i.e., water and Xanthan gum.

## 1.7. Trailing edge ejection - leading edge ejection - complete ejection Experimental Test Procedures

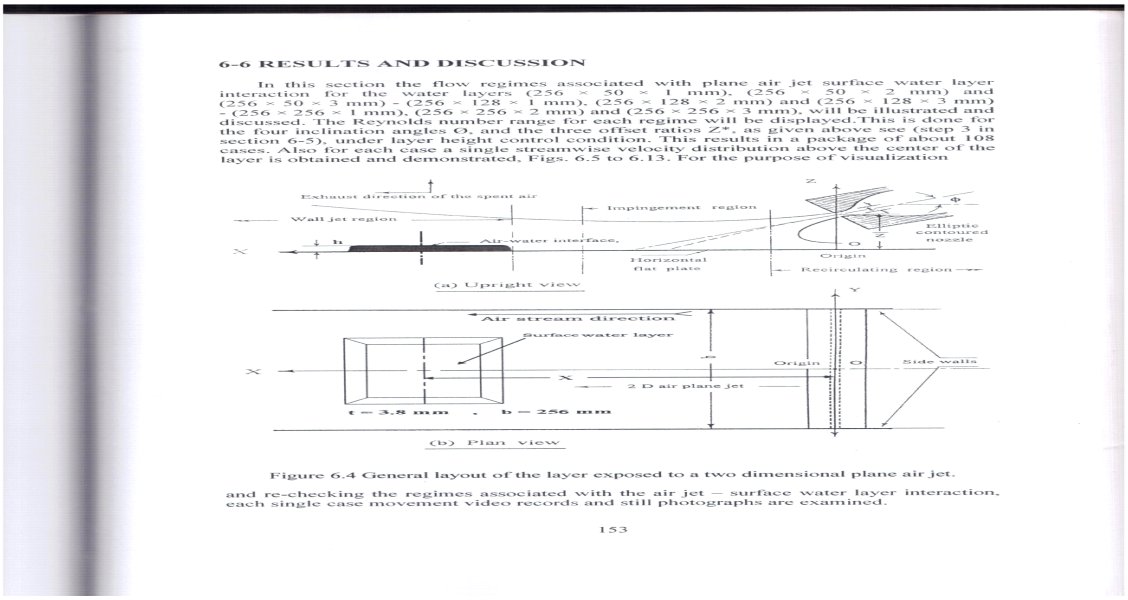

6-6 RESULTS AND DISCUSSION

In this section the flow regimes associated with plane air jet surface water layer interaction for the water layers (256 × 50 × 1 mm), (256 × 50 × 2 mm) and (256 × 50 × 3 mm) - (256 × 128 × 1 mm), (256 × 128 × 2 mm) and (256 × 128 × 3 mm) - (256 × 256 × 1 mm), (256 × 256 × 2 mm) and (256 × 256 × 3 mm), will be illustrated and discussed. The Reynolds number range for each regime will be displayed.This is done for the four inclination angles Φ, and the three offset ratios Z*, as given above see (step 3 in section 6-5), under layer height control condition. This results in a package of about 108 cases. Also for each case a single streamwise velocity distribution above the center of the layer is obtained and demonstrated, Figs. 6.5 to 6.13. For the purpose of visualization



Figure 6.4 General layout of the layer exposed to a two dimensional plane air jet.

and re-checking the regimes associated with the air jet – surface water layer interaction, each single case movement video records and still photographs are examined.

153

In order to establish the different hydrodynamic physical regimes associated with the interaction between plane air jet and surface water layer, the following experimental steps are carried out:

1. Selecting and fixing the wall jet regime through the adjustment of inclination angle φ, offset ratio Z* and the impingement plate horizon. The distance "X" from the nozzle exit to water layer thickness, Fig. 3. As a result of preliminary tests, it is found that wall jet regime had been accurately defined to start at a distance of 47 mm from nozzle exit. So, the water layer center must be located at a pre-determined distance

to permit water layer size variation. The distance X = 175 mm is, therefore, determined and chosen for water layer center location. The water layer center will be fixed at such distance.

2. Measuring of ambient conditions, atmospheric pressure (Patm) and atmospheric temperature (Tatm). These measurements are carried out prior and after each experimental run.

3. Injection of water layer at the location of distance X, defined from step 1, taking into consideration the variation of layer height which usually happened and the four inclination angles (φ = 0°, 15°, 30° and 45°) associated with three offset ratios (Z* =0.5, 2, 3.5) and three layer heights (lmm, 2mm and 3mm) were used. For each single angle, offset ratio and water layer dimensions, three variable heights are examined in accord with the previous concluded remarks and preliminary tests. A 5 cm3 syringe is used to inject the different size water layers onto the flat plate. The layer volume is calculated through measuring the length, width and height of the layer (L x c x h) and is checked through measuring the injected water volume from the syringe scale.

4. The layer height at its center is measured using a level probe (Vernier caliper) of sensitivity ±0.05 mm. If the layer height is less or more than the specified height the syringe is used to adjust the layer height. The layer height, which varied from 1 mm to3mm, was measured accurately to within ±0.07 mm (human and caliper error), while-0.2 mm was allowed for the evaporation error.

5. Starting the air flow at a lower mass flow rate and increasing it until a steady state is reached at the fixed Reynolds number (Rej≈ 1500). The traverses are made for measuring the stream wise velocity distribution over the layer surface center. During this step the layer is exposed to evaporation. So, after finishing the velocity distribution traverse measurements over the layer volume, the layer volume is read and justified using the 5 cm3 syringe and the caliper, to recover any disorders.

6. Since the surface water layer is subjected to evaporation, i.e. "h" is a function of time, it was therefore determined that the time interval for step 7 should not exceed 10% of the total evaporation time of the layer. In this way, the physical dimensions affecting the hydrodynamic regimes are believed to remain almost unaltered.

### 1.7.1. Results and Discussion

In this section, the flow regimes associated with plane air jet surface water layer interaction for the water layers (256 x 50 x 1 mm), (256 x 50 x 2 mm), (256 x 50 x 3 mm), (256 x 128 x 1 mm), (256 x 128 x 2 mm), (256 x 128 x 3 mm), (256 x 256 x 1 mm), (256 x 256 x 2 mm) and (256 x 256 x 3 mm), will be illustrated and discussed. This is done for the four inclination angles φ, and the three offset ratios Z*, as given above see (step 3 in procedures), under layer height control condition. This results in a package of about 108cases. Also, for each case a single stream wise velocity distribution above the center of the layer is obtained and demonstrated. It is anticipated that working with layers of different heights at different inclination angles and different offset ratios would certainly share in reasons leading to the disturbance occur in the sequence of flow regimes. Different flow regime patterns are shown in table 4. It shows the flow regime pattern sequence as Reynolds number increases. Plates 1 to 9illustrate the flow regimes sequence for each single case. The water velocity for each single case is measured, see table 5. Considering individual plates would shed more light on details of every single case.

Table 4 Flow regime numbers and its corresponding patterns.

| Flow regime no. | Flow regime patterns |
|---|---|
| 1 | semi stagnant layer |
| 2 | small scale disturbance |
| 3 | attenuation for vortex motion |
| 4 | large scale disturbance |
| 5 | vortex motion |
| 6 | fast short wave "surface ripples" |
| 7 | fast short waves with notable amplitude "nonlinear dispersive waves" |
| 8 | slow long waves |
| 9 | trailing edge ejection |
| 10 | leading edge ejection |
| 11 | fully ejected layer |

Table5. Water velocity for each single case in mm/sec.

| | ϕ | 0° | | | 15° | | | 30° | | | 45° | | |
|---|---|---|---|---|---|---|---|---|---|---|---|---|---|
| | Z* | 0.5 | 2 | 3.5 | 0.5 | 2 | 3.5 | 0.5 | 2 | 3.5 | 0.5 | 2 | 3.5 |
| Plate number | # 1 | 8.55 | 9.2 | 5.9 | 4.9 | 8.9 | 2.6 | 1.01 | 7.9 | 8.8 | 1.04 | 8.4 | 6.8 |
| | # 2 | 2.9 | 5.3 | 4 | 9.9 | 1.5 | 5.6 | 8.6 | 6.2 | 6.6 | 6.1 | 6.7 | 6.4 |
| | # 3 | 3.9 | 7.6 | 7.1 | 1.5 | 7.7 | 6.7 | 6 | 5.8 | 5.1 | 6.7 | 8.6 | 8.1 |
| | # 4 | 9.5 | 7.5 | 6.04 | 4.1 | 7.3 | 8.6 | 4.5 | 7.9 | 2.9 | 4.5 | 8.1 | 5.7 |
| | # 5 | 2.9 | 3.6 | 4.3 | 3.3 | 4.9 | 3.5 | 3.3 | 6.2 | 3.7 | 6.9 | 5.5 | 4.2 |
| | # 6 | 2.9 | 2.8 | 2.6 | 3 | 2.6 | 1.8 | 3.3 | 5.3 | 2.9 | 4.2 | 3.6 | 3.11 |
| | # 7 | 3.4 | 2.7 | 4.7 | 4.4 | 4.3 | 5.3 | 4.8 | 5.5 | 2.9 | 4.3 | 4.5 | 3.8 |
| | # 8 | 1.7 | 2.5 | 5.3 | 3.8 | 3.2 | 3.8 | 3.4 | 3.2 | 3.1 | 4.3 | 3.8 | 3.5 |
| | # 9 | 2.6 | 1.9 | 2.5 | 2.9 | 2.6 | 2.9 | 3.9 | 2.5 | 4.1 | 5.1 | 4.1 | 6.4 |

Referring to plate #1, the water layer (256 x 50 x 1 mm) is considered. At φ = 0 and Z* = 0.5 and 3.5, all the regimes appear. While at Z* = 2, slow long waves begin to appear before the trailing edge ejection regime. This is perhaps due to that the layer height is small causing more sticking for the layer with plate, which may cause delay in the waves. Also, if fast short waves with amplitude regime are left for a relatively long period under the air jet effect it affects the previous regime turns it to the slow long waves regime. At φ = 15°, all the regimes appeared. At φ = 30° and φ = 45°, leading edge ejection appears faster than trailing edge ejection. In the first case, the leading edge ejection regime appeared after the fast short waves regime and in the second case the leading edge ejection appeared after the vortex motion regime and in both cases the slow long wave's regime did not appear. Here, it can be assumed that both inclination angles 30° and 45° are the best weapon for ejection, since these two angles useless air for layer full ejection. This means less power consumption in systems, and profits in industry using

these angles. It can, however, be concluded that the inclination angle affects the leading edge ejection regime by increasing impingement angle φ.

Plate #1. Flow regimes associated with the (256 x 50 x 1 mm) water layer.

| Plate #1 | Flow regimes sequence | | | | | | | | | | | |
|---|---|---|---|---|---|---|---|---|---|---|---|---|
| ϕ | 0° | | | 15° | | | 30° | | | 45° | | |
| Z* | 0.5 | 2 | 3.5 | 0.5 | 2 | 3.5 | 0.5 | 2 | 3.5 | 0.5 | 2 | 3.5 |
| Flow regimes sequence | 1 | 1 | 1 | 1 | 1 | 1 | 1 | 1 | 1 | 1 | 1 | 1 |
| | 2 | 2 | 2 | 2 | 2 | 2 | 2 | 2 | 2 | 2 | 2 | 2 |
| | 3 | 3 | 3 | 3 | 3 | 3 | 3 | 3 | 3 | 3 | 3 | 3 |
| | 4 | 4 | 4 | 4 | 4 | 4 | 4 | 4 | 4 | 4 | 4 | 4 |
| | 5 | 5 | 5 | 5 | 5 | 5 | 5 | 5 | 5 | 5 | 5 | 5 |

| | | | | | | | | | | | | |
|---|---|---|---|---|---|---|---|---|---|---|---|---|
| | 6 | 6 | 6 | 6 | 6 | 6 | 6 | 6 | 6 | 10 | 10 | 10 |
| | 7 | 8 | 7 | 7 | 7 | 7 | 10 | 10 | 10 | 6 | 6 | 6 |
| | 9 | 9 | 9 | 9 | 9 | 9 | 7 | 7 | 7 | 7 | 7 | 7 |
| | 8 | 10 | 8 | 8 | 8 | 8 | 9 | 9 | 9 | 9 | 9 | 9 |
| | 10 | 11 | 10 | 10 | 10 | 10 | 11 | 11 | 11 | 8 | 11 | 11 |
| | 11 | | 11 | 11 | 11 | 11 | | | | 11 | | |

For water layers with higher thicknesses (256 x 50 x 2 mm), plate #2, in the cases (φ = 0°, Z* = 0.5, 2), the slow long waves are seen to appear after trailing edge ejection. This refers to the work done by air on the water layer surface that expands the layer. It decreases its height and this makes the thin layer to behave the same like the 1 mm height. So, slow long waves occur. It must be taken into consideration that the case (φ = 0°, Z* = 3.5) is the best since the least amount of air is consumed. For the cases (φ = 15°, Z* = 0.5, 2, 3.5), it is clear that the case (φ = 15°, Z* = 0.5) is being the best compared with the other two cases associated with offset ratios Z* = 2, 3.5 for it the least amount of air is consumed for full ejection. The other cases associated with the inclination angles 30° and 45° are characterized by normality in regimes sequence.

Plate #8. Flow regimes associated with the (256 x 256 x 2 mm) water layer.

| Plate #8 | Flow regimes sequence | | | | | | | | | | | |
|---|---|---|---|---|---|---|---|---|---|---|---|---|
| ϕ | $0^o$ | | | $15^o$ | | | $30^o$ | | | $45^o$ | | |
| Z* | 0.5 | 2 | 3.5 | 0.5 | 2 | 3.5 | 0.5 | 2 | 3.5 | 0.5 | 2 | 3.5 |
| Flow regimes sequence | 1 | 1 | 1 | 1 | 1 | 1 | 1 | 1 | 1 | 1 | 1 | 1 |
| | 2 | 2 | 2 | 2 | 2 | 2 | 2 | 2 | 2 | 2 | 2 | 2 |
| | 3 | 4 | 3 | 3 | 3 | 3 | 3 | 3 | 3 | 3 | 3 | 3 |

| | | | | | | | | | | | | |
|---|---|---|---|---|---|---|---|---|---|---|---|---|
| | 4 | 3 | 4 | 4 | 4 | 4 | 4 | 4 | 4 | 4 | 4 | 4 |
| | 5 | 10 | 5 | 5 | 5 | 5 | 5 | 5 | 10 | 5 | 5 | 5 |
| | 6 | 5 | 6 | 6 | 6 | 10 | 6 | 10 | 5 | 10 | 10 | 10 |
| | 10 | 6 | 10 | 10 | 10 | 6 | 7 | 6 | 6 | 6 | 6 | 6 |
| | 7 | 7 | 7 | 7 | 7 | 7 | 10 | 7 | 7 | 7 | 7 | 7 |
| | 9 | 9 | 9 | 9 | 9 | 9 | 9 | 9 | 9 | 9 | 9 | 9 |
| | 11 | 11 | 11 | 8 | 8 | 8 | 11 | 8 | 11 | 8 | 8 | 11 |
| | | | | 11 | 11 | 11 | | 11 | | 11 | 11 | |

Finally, (256 x 256 x 3 mm) water layers, shows normality in the regimes sequence except in the cases (φ = 30°, Z* = 0.5, h =3) and (φ = 30°, Z* = 2, h = 3), plate #9. Here, leading edge ejection occurs after fast short waves and this may refer to the effect of inclination angle. Also, as previously mentioned, increasing the layer height causes higher sensitivity for layer surface interaction with the air stream that allows the flow regimes to appear earlier, plates #7, #8 and #9.

Plate #9. Flow regimes associated with the (256 x 256 x 3 mm) water layer.

| Plate #9 | Flow regimes sequence | | | | | | | | | | | |
|---|---|---|---|---|---|---|---|---|---|---|---|---|
| ϕ | 0° | | | 15° | | | 30° | | | 45° | | |
| Z* | 0.5 | 2 | 3.5 | 0.5 | 2 | 3.5 | 0.5 | 2 | 3.5 | 0.5 | 2 | 3.5 |
| Flow regimes sequence | 1 | 1 | 1 | 1 | 1 | 1 | 1 | 1 | 1 | 1 | 1 | 1 |
| | 2 | 2 | 2 | 2 | 2 | 2 | 2 | 2 | 2 | 2 | 2 | 2 |
| | 3 | 3 | 3 | 3 | 3 | 3 | 3 | 3 | 3 | 3 | 3 | 3 |
| | 4 | 4 | 4 | 4 | 4 | 4 | 4 | 4 | 4 | 4 | 4 | 4 |
| | 5 | 5 | 5 | 5 | 5 | 5 | 5 | 5 | 5 | 5 | 5 | 5 |
| | 6 | 6 | 6 | 6 | 6 | 6 | 6 | 6 | 6 | 6 | 6 | 6 |
| | 7 | 7 | 7 | 7 | 7 | 7 | 10 | 10 | 7 | 7 | 7 | 7 |
| | 9 | 9 | 9 | 9 | 9 | 9 | 7 | 7 | 9 | 9 | 9 | 9 |
| | 10 | 10 | 10 | 10 | 10 | 10 | 9 | 9 | 10 | 10 | 10 | 10 |
| | 11 | 8 | 8 | 11 | 11 | 11 | 11 | 11 | 8 | 8 | 8 | 11 |
| | | 11 | 11 | | | | | | 11 | 11 | 11 | |

The most attractive note from all the cases is that the uniform velocity distribution phenomenon occurred in the velocity distribution profiles or in the wall jet region over the impingement flat plate in the impingement region. This refers to that the friction and disturbance to air jet near the flat surface is enhanced due to presence of water layer, since the measurements begin from positions over the layers at a distance from the impingement plate not less than 1.45 mm and not more than 3.45 mm. Figs. 8 to 43 show velocity profiles in the impingement regime over water layers.

# Chapter two

# 2. Theoretical topics

Observation from the present experimental work is the basic motivation behind the present theoretical approach. this section is preferred to be reviewed firstly, before the observation section itself, to avoid the discontinuity and/or interference during the investigation of such observations. Surface tension, water waves (surface ripples), and vortex motion are mainly the three topics that will be treated hereafter.

## 2.1. Surface tension and Surface Energy

- Properties of liquid Surfaces

A molecule in the interior of a liquid is completely surrounded by other molecules, and so, on the average, it is attracted equally in all directions. On a molecule in the surface of a liquid, however, there is a resultant attraction inward, the number of molecules per unit volume is greater in the bulk of the liquid than in the vapor. As a consequence of this inward pull the surface of a liquid always tends to contract to the smallest possible area; it is for this reason that drops of liquid and bubbles of gas in a liquid become spherical, the surface being then a minimum for the given volume. In order to extend the area of the surfaces it is obviously necessary to do work to bring the molecules from the bulk of the liquid into the surface against the inward attractive force; the work required to increase the area by $1\times10^{-4}m^2$ Is called the free surface energy [9]. The tendency for a liquid to contract may be regarded as a consequence of its possession of free energy since approach to equilibrium is always accompanied by a diminution of free energy.

As a result of the tendency to contract, a surface behaves as if it was in a state of tension, and it is possible to ascribe a definite value to this surface tension, which isthe same at every point and all directions along the surface of the liquid. It is given the symbol б and may be defined as the force in dynes acting at right angles to any line of $1\times10^{-2}$ length in the surface. The work done in extending the area of a surface by $1\times10^{-4}m^2$ equal to the surface tension.

The existence of a surface implies a separation between two media, e.g., liquid and gas and the surface tension are dependent on the nature of both substances. As a general rule the recorded values of the surface tensions of liquids are those for the interface between the liquid and air saturated with the vapor.

The work required to enlarge the surface of separation between two immiscible or partially miscible liquids are called the interfacial surface energy and is often expressed as the interfacial tension. The interfacial tension between two liquids is generally less than the larger of the two surface tensions; the mutual attraction across the interface between the molecules of one liquid and those of the other tends to reduce the inward pull of the molecules in the surface by those of its own kind. The tensions at liquid- solid interfaces are of theoretical importance, but very little quantitative information concerning them is yet available, [9].

• Contact angle and wetting.

Suppose a liquid L rests on the surface of a solid S and comes to equilibrium with the angle of contact, measured in the liquid, equal to б, as shown in Fig. 4.6 where G is the gas, generally air, in contact with the solid and liquid. At equilibrium the force acting at the interfaces must balance, and assuming that these can be represented by surface tensions acting in the direction of the surfaces, it follows that:

$$б_{GS} = б_{LS} . б_{GL} \cos Ө \quad (4\text{-}5)$$

Where $б_{GS}$ $б_{LS}$ and $б_{GL}$ are the surface energies, or tensions of the gas-solid, liquid- solid and gas-liquid surfaces, respectively. The contact angle Ө thus depends on the three interfacial tensions, but whether it is greater or less than 90° is governed by the relative magnitudes of $б_{GS}$ and $б_{LS}$

• The Dupre Equation.

The subject of wetting and of the magnitude of the contact angle may be considered from another point of view. When the surface between L and S in Fig.4.6 is diminished by $1x10^{1}m^{2}$the interfaces between G and S, and between G and L are both increased by

$1x10^{-4}$ m², and the resultant work done is $б_{GS}$+ $б_{GL}$- $б_{LS}$. This work is a measure of the energy required to separate the solid from the liquid and is called the work of adhesion between solid and liquid and is given the symbol $W_{LS}$, thus:

$W_{LS} = б_{GS} + б_{GL} - б_{LS}$

This is a form of the equation first deduced by Dupre (1860) and generally known by his name [9].

Since the work of cohesion of the liquid is proportional to $б_{GL}$, so if equations (4-5) and (4-6) are now combined it is seen that:

$W_{LS} = б_{GS} (1+ \cos Ө)$ (4-7)

So that the contact angle Ө depends on the relative values of the adhesion work of the solid and liquid and the cohesion work of the liquid, i.e., attraction of the solid and liquid, and between the molecules of the liquid themselves. Provided the cohesion work is less than half that of adhesion, i.e. the attraction of the liquid for the solid is more than half that for itself, Ө is less than 90° and wetting is said to occur. As is to be expected, from general considerations, wetting of a solid by a liquid is therefore the result of a relatively high degree of attraction between the molecules of the solid and the liquid,

## 2.2. Water Waves

• surface gravity waves

Even an introductory treatment of waves in fluids must survey dispersion effects: a complicated group of phenomena found in a large majority of wave- propagation systems in fluids; namely, those in which the wave speed c varies with the wavelength and possibly also with the direction of propagation. Thus, even while amplitudes remain very small so that a linear theory can be used, the propagation velocity takes different values for different sinusoidal components of the general disturbance.

The present section is primarily concerned with giving a general review of the linear theory applied to dispersion effects. The particular wave systems described in this

section, mainly gravity waves, although of substantial importance in their own right, are used to exemplify dispersion phenomena; all nonlinear effects are omitted. The existence of fluids both in liquid and gaseous phases allows also a quite different type of stable equilibrium with heavier fluid underlying lighter: one is homogeneous liquid (for example, water) separated by a horizontal surface of a homogeneous gas above it (for example, air). The density variation is then discontinuous and is confined to a surface: the water surface. (Or in general the gas-liquid interface).

Disturbances to this state of equilibrium take the form of surface gravity waves, that cannot move far from the surface for deep water not more than one wavelength away. Accordingly, their propagation over distances of many wavelengths is in the horizontal directions only. Since the existence of a vertical restoring force due to gravity can make no distinction between different horizontal directions, the waves are isotropic (all propagation directions are equal). The effective fluid inertia, however, associated with a depth of penetration of disturbances depending upon wavelength, causes dispersion: a dependence of wave speed upon wavelength, Lighthill [10]. In this general linear theory of gravity waves on a homogeneous body of water, compressibility proves to be negligible so that water density may be taken as a constant $p_w$

The undisturbed pressure distribution is hydrostatically determined

$$P_w=p_a-p_wgz \qquad (4\text{-}8)$$

Where $p_a$ is the atmospheric pressure. The excess pressure due to disturbance is defined as

$$P_e=P-P_w. \qquad (4\text{-}9)$$

The linearized momentum equation may be written as

$$P_wp_c \qquad (4\text{-}10)$$

Where the nonlinear term in the acceleration, u.u, has been neglected and it is deduced by taking the curl" that on linear theory the vorticity field is independent of the

rotational part of the velocity field, induced by this stationary vorticity field, is independent of time, has $P_e = 0$ by equation (4-10), and therefore does not disturb the flatness of the water surface. The remaining part of the velocity field is irrotational and so can be written as the gradient of a velocity potential. Only this part disturbs the water surface or exhibits the fluctuations associated with wave propagation The equation of continuity for an incompressible fluid is giving for this irrotational propagating part of the velocity field Laplace's equation:

$^2=0$ (4-11)

Although Laplace's equation can never describe the propagation of waves in any fluid wholly bounded by stationary surfaces, it can do so in combination with the conditions satisfied at a free water surface. These require that:

$P_e = p_w g$ (4-12)

On the disturbed water surface, Fig. 4.7:

# Chapter three

## 3. Experimental analysis

### 3.1. Experiment test rig

illustrates the experimental set-up. A pressure head station for compressed air consists mainly of an Ingersoll-Rand 63kW, three phase screw compressor delivering 8.5 m3 /min compressed air, storage tank of 3 m3 capacity (max. pressure = 8 – 10 bar), air filters, and mass refrigeration air dryer unit. The compressed air passes through a one-inch stainless steel ball valve at a pressure range of (6 - 7) bar, then into a pressure regulator of regulation range (0 – 12) bar, to an orifice meter, which is assembled according to standard dimensions for the pressure tapping ports. Air leaving the metering system is passed through a seven outlet distributor; identical seven looped flexible hoses transfer the compressed air from the distributor to the inlet of a wide angle diffuser, followed by a plenum chamber, leading to the jet nozzle assembly. The distributor looped in many circles to act as a damping volume for the pressure fluctuations caused by air. It helps to

create a laminar air velocity profile and this makes the readings more stable, At the air entrance to, and exit from the metering system, a cone shape is formed to avoid energy

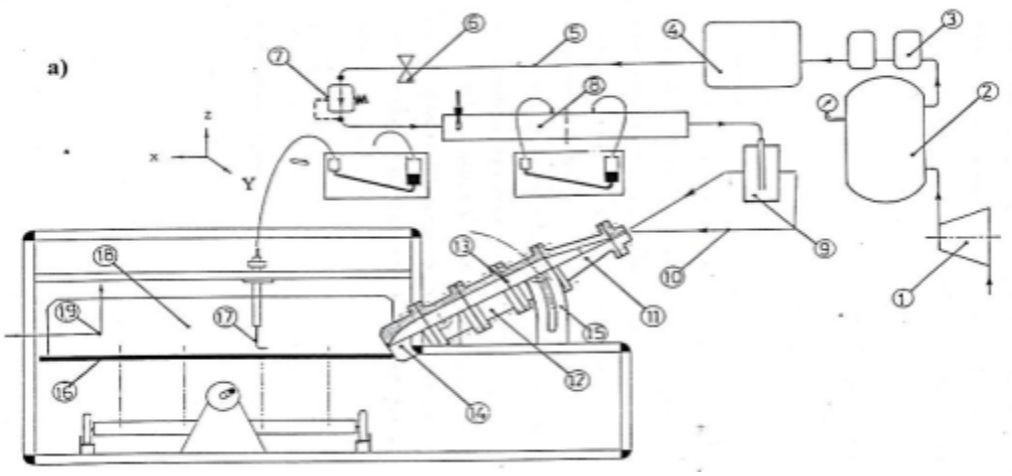


1. Screw compressor. 2. Pressure tank. 3. Air filters.
4. Mass refrigeration air dryer. 5. Main supply pipe. 6. Main supply valve.
7. Pressure regulator. 8. Orifice meter. 9. Seven outlet distributor.
10. Flexible hoses. 11. Wide angle diffuser. 12. Plenum chambers.
13. Screens. 14. Elliptic contoured nozzle. 15. Inclination angle adjustment mechanism. 16. Impingement plate. 17. Pitot-tube attached to an inclined manometer. 18. Side walls. 19. Exhaust of the spent air

## 3.2. Measurements and Instrumentation

For these experiments, a Pitot tube, with accuracy limits of ±0.125 mm, is calibrated against an “Air flow- PVM100” micro manometer for pressure and velocity measurements. The used inclined-manometer is filled with red dye oil (Sp.Gr. = 0.826). The impingement plate is prepared to ease the process of measuring and photographing, by a drawn net of 5 cm squares made of horizontal and vertical lines. The impinging region is classified into three different regions inside a large square, shown in Figs. 4 and 5, near to the nozzle at the beginning of the plate. The first is 256 x

50 mm layer. The second is 256 x 128 mm layer. The third is 256 x 256 mm layer. Atmospheric pressure is measured by a barometer.

## 3.3. Preliminary tests on nozzle exit velocity

The nozzle with dimensions (b = 256 mm and t = 3.8 mm) is designed to be so close to real situation in industry. Fig. 6 shows the nozzle assembly with respect to the impinging plate. Exit velocity measurements are conducted to confirm the uniformity of the exit velocity distribution through the nozzle mouth (b x t). This is done by measuring velocity head of a network consists of (7 x 9) points distributed in a uniform manner in the (x – z) plane.

## 3.4. Test Procedures

In order to establish the different flow regimes associated with the plane air jet impinging on a flat plate, the following experiment steps are carried out:

1. Adjustment of geometrical parameters to the required settings, shown in Fig. 8. They include inclination angles $\phi$ = 0o, 15o, 30o, 45o, offset ratios Z* = ($\overline{Z}$/t) = 0.5, 2, 3.5, and the impinging plate's horizontal mounting.
2. Measurement of ambient conditions; pressure (Patm) and temperature (Tatm).
3. Start the air flow at a desired Reynolds number Rej; through adjustment of the corresponding pressure regulator reading. Wait until steady state condition is established. Steady state condition and Rej value are to be checked by measuring the center line jet exit velocity at nozzle mouth Uj. In the present experiment, the value of Reynolds number is selected as Rej ≈ 1500.
4. Measurement of reattachment distance XR, to avoid recirculating regions, Fig. 9, by moving the Pitot tube gradually along the center line of the impinging plate with a verified notation that the probe is tangent to the plate. Until the manometer reading just exceeds the zero reading. The horizontal distance

between the probe nose at this location and the point vertically viewed from the nozzle exit midpoint represents the reattached distance XR.

5. Using Pitot tube traverses measurements are made of velocity distributions U = U(Z) at different stations, as shown in Fig. 9. In order to conform to experiments, the selected stations were therefore related to the size of considered layers there (256 x 50, 256 x 128, and 256 x 256). Nominally three station for each layer are considered (leading edge, middle of layer, and trailing edge), as shown in Fig. 10. These stations are selected with a separation distance (25, 64, and 128 mm respectively) to define accurately the wall jet regime related to certain values of Rej, ϕ, Z*. 6- Repeat of steps 1, 2, 4, and 5 for other values of ϕ, Z*.

# Chapter Four

## 4. Results and discussion

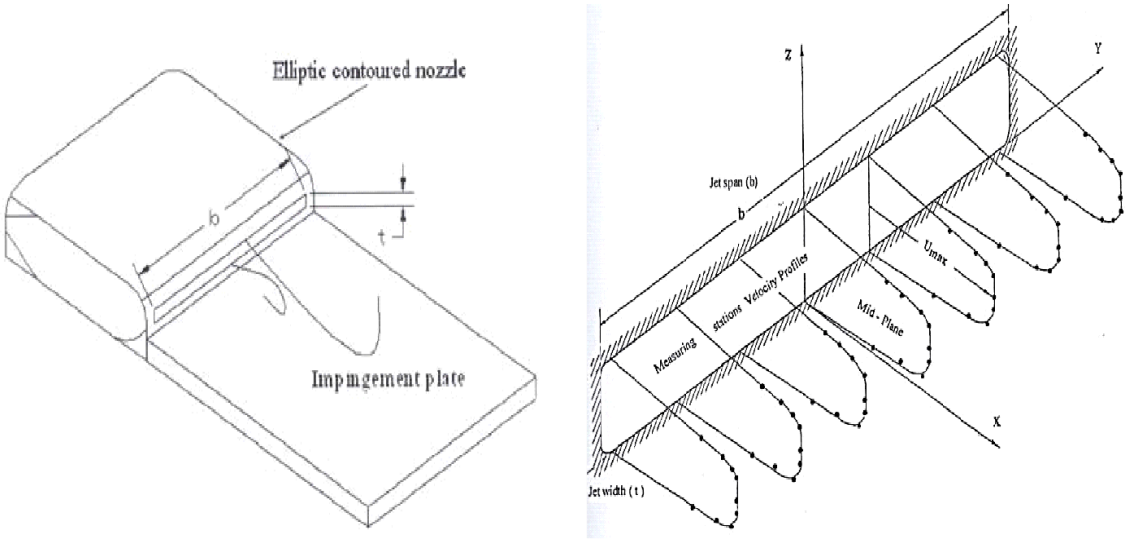


## 5. Conclusions

A parametric experimental study is carried out to investigate the effect of inclination angle φ and offset ratio Z* on the wall jet resulting from the impingement of a plane air jet onto a flat plate. Results in terms of velocity distributions for four inclination angles (φ = 0, 15, 30, and 45), three offset ratios (Z* = 0.5, 2, and 3.5) and one

Reynolds number (Rej = 1500) are obtained. Followings are the achieved conclusions from these results:

1- Wall jet regimes are achieved for all test cases at a distance not more than XR

RR = 34 mm.

2- Both of the inclination angle φ and offset ratio Z* are found to have substantial effects on the

wall behavior.

3- The package combination (φ = 15, 45 and Z* = 2) seems to be the most attractive among the other investigated angles, since it represents the more efficient utilization of the jet momentum.

## References

[1] Narayanan, V., J. Seyed-Yagoobi, and R.H. Page, An experimental study of fluid mechanics and heat transfer in an impinging slot jet flow. International Journal of Heat and Mass Transfer, 2004. 47: p. 1827–1845.

[2] Baydar, E. and Y. Ozmen, An experimental and numerical investigation on a confined impinging air jet at high Reynolds numbers. Applied Thermal Engineering, 2005. 25: p. 409–421.

[3] Han, B. and R.J. Goldstein, Jet-impingement heat transfer in gas turbine systems, in Annals of the New York Academy of Sciences. 2001. p. 147-161.

[4] Polat, S., Heat and mass transfer in impingement drying. Drying Technology, 1993. 11(6): p. 1147-1176.

[5] Viskanta, R., Heat transfer to impinging isothermal gas and flame jets. Experimental Thermal and Fluid Science, 1993. 6(2): p. 111-134.

[6]. Gardon, R. and J.C. Akfirat, Heat transfer characteristics of impinging two-dimensional air jets. J. Heat Transfer, 1966. 88: p. 101-108.

[7] Gardon, R. and J. Cobonpue, 1962: p. 454-460.

[8] Sarkar, A., et al., Fluid flow and heat transfer in air jet impingement in food processing. Journal of Food Science, 2004. 69(4): p. CRH113-CRH122.

[9] Fabbri, M., S. Jiang, and V.K. Dhir, A comparative study of cooling of high power density electronics using sprays and microjets. Journal of Heat Transfer, 2005. 127(1): p. 38-48.

[10] Anwarullah, M., V.V. Rao, and K.V. Sharma, Experimental investigation for enhancement of heat transfer from cooling of electronic components by circular air jet impingement. Heat and Mass Transfer, 2012. 48(9): p. 1627-1635.

[11] Martin, H., Heat and Mass Transfer between Impinging Gas Jets and Solid Surfaces, in Advances in Heat Transfer. 1977. p. 1-60.

[12] Carlomagno, G.M. and A. Ianiro, Thermo-fluid-dynamics of submerged jets impinging at short nozzle-to-plate distance: A review. Experimental Thermal and Fluid Science, 2014. 58(): p. 15-35.

[13] Hall, J.W. and D. Ewing, On the dynamics of the large-scale structures in round impinging jets. Journal of Fluid Mechanics, 2006. 555: p. 439-458.

[14]. Harmand, S., et al., Review of fluid flow and convective heat transfer within rotating disk cavities with impinging jet. International Journal of Thermal Sciences, 2013. 67: p. 1-30.

[15]. Polat, S., et al., Numerical flow and heat transfer under impinging jets: A review. Annual Review of Numerical Fluid Mechanics and Heat Transfer, 1989. 2: p. 157-197.

[16]. Kristiawan, M., et al., Wall shear rates and mass transfer in impinging jets: Comparison of circular convergent and cross-shaped orifice nozzles. International Journal of Heat and Mass Transfer, 2012. 55(1–3): p. 282-293.

[17]. Meslem, A., et al., Flow dynamics and mass transfer in impinging circular jet at low Reynolds number. Comparison of convergent and orifice nozzles. International Journal of Heat and Mass Transfer, 2013. 67: p. 25-45.

[18]-Coles, D. W., “Jet-engine Exhaust Noise from Slot Nozzles,” Tech. Rep. D-60, NASA (National Aeronautics and SpaceAdministration), September 1959.

[19]-Lighthill, M. J., “On Sound Generated Aerodynamically – I. General Theory,” Proceedings of the Royal Society of London.Series A. Mathematical and Physical Sciences, Vol. 211, No. 1107, March 1952, pp. 564–587.

[20]-Lighthill, M. J., “On Sound Generated Aerodynamically – II. Turbulance as a Source of Sound,” Proceedings of the RoyalSociety of London. Series A. Mathematical and Physical Sciences, Vol. 222, No. 1148, February 1954, pp. 1–32.

[21]-Lighthill, M. J., “Sound Generated Aerodynamically,” Proceedings of the Royal Society of London. Series A. Mathemat-ical and Physical Sciences, Vol. 267, No. 1329, November 1962, pp. 147–182.

[22]-Kouts, C. and Yu, J. C., “Far Noise Field of a Two-dimensional Subsonic Jet,” AIAA Journal, Vol. 13, No. 8, August1975, pp. 1031–1035.

[23]-Larsen, P. N., Noise Generated by Air Jets from a Rectangular Slit, Ph.D. thesis, Technical University of Denmark, 1983.

[24]-Bjørnø, L. and Larsen, P. N., “Noise of Air Jets from Rectangular Slits,” Acustica, Vol. 54, No. 5, March 1984, pp. 247–256.

[25]-Munro, S. E. and Ahuja, K. K., “Application of Circulation Control Technology to Airframe Noise Reduction,” Tech.Rep. NASA ID - 20030065823, Georgia Institute of Technology, May 2003.

[26]-Tam, C. K. W., “Influence of Nozzle Geometry on the Noise of High-speed Jets,” AIAA Journal, Vol. 36, No. 8, August1998, pp. 1396–1400.

[27]-Tam, C. K. W. and Zaman, K. B. M. Q., “Subsonic Jet Noise from Non-axisymmetric and Tabbed Nozzles,” 37thAerospace Sciences Meeting and Exhibit, American Institute of Aeronautics and Astronautics, January 1999.

[28]-Tam, C. K. W. and Pastouchenko, N., “Noise from the Fine Scale Turbulence of Nonaxisymmetric Jets,” 7th AIAA/CEASAeroacoustics Conference and Exhibit, Aeroacoustics Conferences, American Institute of Aeronautics and Astronautics, May2001.

[29]-Kanjere, K., Desvard, L., Nicolas, F., Henrywood, R. H., and Agarwal, A., “Empirical Modelling of Noise from HighAspect Ratio Jets,” 5th International Conference on Jets Wakes and Separated Flow, Stockholm, June 2015.

[30]-Mi, J. and Nathan, G. J., “Statistical Properties of Turbulent Free Jets Issuing from Nine Differently-shaped Nozzles,” Flow, Turbulence and Combustion, Vol. 84, 2010, pp. 583–606.

[31]-Mi, J., Deo, R. C., and Nathan, G. J., “Characterisation of Turbulent Jets from High-aspect-ratio Nozzles,” Physics ofFluids, Vol. 17, No. 6, 2005, pp. 068102.

[32]-Deo, R. C., Mi, J., and Nathan, G. J., “The Influence of Nozzle Aspect Ratio on Plane Jets,” Experimental, Thermaland Fluid Science, Vol. 31, 2007, pp. 825–838.

[33]-Deo, R. C., Mi, J., and Nathan, G. J., “The Influence of Nozzle-exit Geometric Profile on Statistical Properties of aTurbulent Plane Jet,” Experimental Thermal and Fluid Science, Vol. 32, No. 2, 2007, pp. 545 – 559.

[33]-Deo, R. C., Mi, J., and Nathan, G. J., “The Influence of Reynolds Number on a Plane Jet,” Physics of Fluids , Vol. 20,No. 7, 2008, pp. 075108.

[34]-Deo, R. C., Experimental Investigations of the Influence of Reynolds Number and Boundary Conditions on a Plane AirJet, Ph.D. thesis, The University of Adelaide, 2005.

[35]-Quinn, W. R., “Turbulent Free Jet Flows Issuing from Sharp-edged Rectangular Slots: The Influence of Slot AspectRatio,” Experimental, Thermal and Fluid Science, Vol. 5, No. 2, March 1992, pp. 203–215.

[36]-Goldschmidt, V. W. and Bradshaw, P., “Flapping of a Plane Jet,” Physics of Fluids, Vol. 16, No. 3, 1973, pp. 354.

[37]George, W. K., Advances in Turbulence, chap. The Self-Preservation of Turbulent Flows and its Relation to InitialConditions, Hemisphere, New York, 1989, pp. 39–37.

[38]George, W. K. and Davidson, L., “Role of Initial Conditions in Establishing Asymptotic Flow Behavior,” AIAA Journal,Vol. 42, No. 3, March 2004, pp. 438–446.

[39]Jordan, P. and Colonius, T., “Wave Packets and Turbulent Jet Noise,” Annual Review of Fluid Mechanics, Vol. 45, 2013,pp. 173–195

[40] Gauntner J, Livingood JNB, Hrycak P, N.A.S.A.T.N. D-, J.W. Guzlntner, P.Hrycuk, Survey of literature on flow characteristics of a single turbulent jet impinging on a flat plate, Washington, DC, 1970, 43.

[41] Hadžiabdić M, Hanjalić K, Vortical structures and heat transfer in a round impinging jet, J. Fluid Mech. 596, 2008, 221–260.

[42] Gardon R, Akfirat JC, The role of turbulence in determining the heat-transfer characteristics of impinging jets, Int. J. Heat Mass Transf. 8, 1965, 1261–1272.

[43] ANSYS, ANSYS FLUENT User's Guide, 15317 (2011) 2498.

[44] Dairay T, Fortuné V, Lamballais E, Brizzi LE, Direct numerical simulation of a turbulent jet impinging on a heated wall, Int. J. Heat Fluid Flow. 764, 2015, 362–394.

[45] Rohlfs W, Haustein HD, Garbrecht O, Kneer R, Insights into the local heat transfer of a submerged impinging jet: Influence of local flow acceleration and vortex-wall interaction, Int. J. Heat Mass Transf. 55, 2012, 7728–7736.

[46] Epelle, E.I.; Gerogiorgis, D.I. A review of technological advances and open challenges for oil and gas drilling systems engineering. AIChE J. 2020, 66, e16842.

[47] Zahid, A.A.; Rehman, S.R.; Rushd, S.; Hasan, A.; Rahman, M.A. Experimental investigation of multiphase flow behavior in drilling annuli using high speed visualization technique. Front. Energy 2018.

[48] Khan, M.S.; Bavoh, C.B.; Partoon, B.; Nashed, O.; Lal, B.; Mellon, N.B. Impacts of ammonium based ionic liquids alkyl chain on thermodynamic hydrate inhibition for carbon dioxide rich binary gas. J. Mol. Liq. 2018, 261, 283–290.

[49] Kamyab, M.; Rasouli, V.; Cavanough, G.; Mandal, S. Challenges of cuttings transport in micro- borehole coiled tubing drilling for mineral exploration. WIT Trans. Eng. Sci. 2013, 81, 109–120.

[50] Kelin, W.; Tie, Y.; Xiaofeng, S.; Shuai, S.; Shizhu, L. Review and analysis of cuttings transport in complex structural wells. Open Fuels Energy Sci. J. 2013, 6, 9–17.

[51] Qasim, A.; Khan, M.S.; Lal, B.; Shariff, A.M. A perspective on dual purpose gas hydrate and corrosion inhibitors for flow assurance. J. Pet. Sci. Eng. 2019, 183, 106418.

[52] Taitel, Y.; Dukler, A.E. A model for predicting flow regime transitions in horizontal and near horizontal gas-liquid flow. AIChE J. 1976, 22, 47–55.

[53] Shojaei, M.J.; Rodríguez de Castro, A.; Méheust, Y.; Shokri, N. Dynamics of foam flow in a rock fracture: Effects of aperture variation on apparent shear viscosity and bubble morphology. J. Colloid Interface Sci. 2019, 552, 464–475.

[54] Mandhane, J.M.; Gregory, G.A.; Aziz, K. A flow pattern map for gas-liquid flow in horizontal pipes. Int. J. Multiph. Flow 1974, 1, 537–553.

[55] Chhabra, R.P.; Richardson, J.F. Prediction of flow pattern for the co-current flow of gas and non-newtonian liquid in horizontal pipes. Can. J. Chem. Eng. 1984, 62, 449–454.

[56] Azarinezhad-Mohammadi, R. A Chemical Based Wet Cold Flow Approach for Addressing Hydrate Flow Assurance Problems. Ph.D. Thesis, Heriot-Watt University , Edinburgh, UK, 2010.

[57] Khan, M.S.; Lal, B.; Bavoh, C.B.; Keong, L.K.; Bustam, A. Influence of ammonium based compounds for gas hydrate mitigation: A short review. Indian J. Sci. Technol. 2017, 10, 1–6.

[58] Al-Safran, E. Investigation and prediction of slug frequency in gas/liquid horizontal pipe flow. J. Pet. Sci. Eng. 2009, 69, 143–155.

[59] Sultan, R.A.; Alfarek, S.; Rahman, M.A.; Zendehboudi, S. CFD and experimental approach on three phase gas-liquid-solid Newtonian fluid flow in horizontal pipes. Int. J. Comput. Methods Exp. Meas. 2018, 7, 33–44.

[60] Zadrazil, I.; Markides, C.N. An experimental characterization of liquid films in downwards co-current gas-liquid annular flow by particle image and tracking velocimetry. Int. J. Multiph. Flow 2014, 67, 42–53.

[61] Cerqueira, R.F.L.; Paladino, E.E.; Ynumaru, B.K.; Maliska, C.R. Image processing techniques for the measurement of two-phase bubbly pipe flows using particle image and tracking velocimetry (PIV/PTV). Chem. Eng. Sci. 2018, 189, 1–23.

[62] Talley, J.D.; Worosz, T.; Kim, S.; Buchanan, J.R. Characterization of horizontal air–water two-phase flow in a round pipe part I: Flow visualization. Int. J. Multiph. Flow 2015, 76, 212–222.

[63] Majumder, S.K.; Ghosh, S.; Kundu, G.; Mitra, A.K. Frictional pressure drop of gas-Newtonian and gas-non Newtonian slug flow in vertical pipe. Int. J. Chem. React. Eng. 2011.

[64] Ehinmowo, A.B.; Cao, Y.; Yeung, H.C. Slug flow in large diameter pipeline—Riser systems: Prediction and mitigation. Covenant J. Eng. Technol. 2018, 2, 1–21.

[65] Majumder, S.K.; Ghosh, S.; Mitra, A.K.; Kundu, G. Gas-Newtonian and gas-non-Newtonian slug flow in vertical pipe, part I: Gas holdup characteristics. Int. J. Chem. React. Eng. 2010.

[66] Abed, E.M.; Ghoben, K. Gas-liquid slug frequency and slug unit length in horizontal pipes. Iraqi J. Mech. Mater. Eng. 2015, 15, 166–180. Appl. Sci. 2020, 10, 3272 26 of 27

[67] Zabaras, G.J.; Shell, E.; Co, P.T. Prediction of Slug Frequency for Gas/Liquid Flows; Society of Petroleum Engineers: Richardson, TX, USA, 1999.

[68] Sultan, R.A.; Rahman, M.A.; Rushd, S.; Zendehboudi, S.; Kelessidis, V.C. CFD analysis of pressure losses and deposition velocities in horizontal annuli. Int. J. Chem. Eng. 2019, 2019, 1–17.

[69] Daza Gómez, M.A.; Ratkovich, N.; Pereyra, E.; Poesio, P. CFD simulations of two-phase gas/non-Newtonian fluid flows in pipes. In Proceedings of the 3rd World Congress on Momentum, Heat and Mass Transfer (MHMT'18), Budapest, Hungary, 12–14 April 2018. 26. Dziubinski, M.; Fidos, H.; Sosno, M. The flow pattern map of a two-phase non-Newtonian liquid-gas flow in the vertical pipe. Int. J. Multiph. Flow 2004, 30, 551–563.

[70] Katzbauer, B. Properties and applications of xanthan gum. Polym. Degrad. Stab. 1998, 59, 81–84.

[71] Bavoh, C.B.; Md Yuha, Y.B.; Tay, W.H.; Ofei, T.N.; Lal, B.; Mukhtar, H. Experimental and modelling of the impact of quaternary ammonium salts/ionic liquid on the rheological and hydrate inhibition properties of xanthan gum water-based muds for drilling gas hydrate-bearing rocks. J. Pet. Sci. Eng. 2019, 183, 106468.

[72] Owusu, E.B.; Tsegab, H.; Sum, C.W.; Padmanabhan, E.; Qasim, A.; Khan, M.S.; Lal, B.; Ismail, M.C.; Rostani, K.; Shojaei, M.J.; et al. Synthesis, characterization, stability and thermal conductivity of multi-walled carbon nanotubes (MWCNTs) and eco-friendly jatropha seed oil based nanofluid: An experimental investigation and modeling approach. J. Mol. Liq. 2019, 293, 6–14.

[73] Tutu, N.K. Pressure fluctuations and flow pattern recognition in vertical two phase gas-liquid flows. Int. J. Multiph. Flow 1982, 8, 443–447.

[74] Drahoš, J.; Cerm ˇ ák, J.; Selucky, K.; Ebner, L. Characterization of hydrodynamic regimes in horizontal two-phase flow: Part II: Analysis of wall pressure fluctuations. Chem. Eng. Process. Process Intensif. 1987, 22, 45–52.

[75] Sun, Z.; Shao, S.; Gong, H. Gas-liquid flow pattern recognition based on wavelet packet energy entropy of vortex-induced pressure fluctuation. Meas. Sci. Rev. 2013, 13, 83–88.

[76] Blaney, S. Gamma Radiation Methods for Clamp-On Multiphase Flow Metering; Cranfield University: Bedford, UK, 2008.

[77] Park, S.H.; Kim, S.D. Characterization of pressure signals in a bubble column by wavelet packet transform. Korean J. Chem. Eng. 2003, 20, 128–132.

[78] De Fang, L.; Liu, R.; Lu, Q.H.; Wang, X.J.; Liang, Y.J. The flow pattern transition identification and interphases force detection of gas-liquid two-phase flow. AASRI Procedia 2012, 3, 534–539.

[79] Elperin, T.; Klochko, M. Flow regime identification in a two-phase flow using wavelet transform. Exp. Fluids 2002, 32, 674–682.